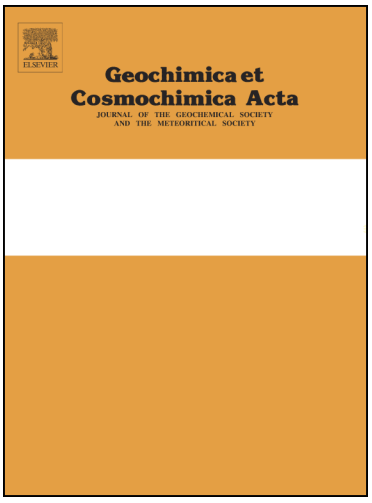

Shock conditions recorded in NWA 8159 martian augite basalt with implications for the impact cratering history on Mars

Tom G. Sharp, Erin L. Walton, Jinping Hu, Carl Agee

PII: S0016-7037(18)30644-6
DOI: https://doi.org/10.1016/j.gca.2018.11.014
Reference: GCA 11009

To appear in: *Geochimica et Cosmochimica Acta*

Received Date: 28 March 2018
Accepted Date: 9 November 2018

Please cite this article as: Sharp, T.G., Walton, E.L., Hu, J., Agee, C., Shock conditions recorded in NWA 8159 martian augite basalt with implications for the impact cratering history on Mars, *Geochimica et Cosmochimica Acta* (2018), doi: https://doi.org/10.1016/j.gca.2018.11.014

Shock conditions recorded in NWA 8159 martian augite basalt with implications for the impact cratering history on Mars

Tom G. Sharp[1], Erin L. Walton[2,3,*], Jinping Hu[4] and Carl Agee[5]

[1]Arizona State University, School of Earth & Space Exploration, Tempe, AZ, 85287-1404, United States.[2]MacEwan University, Department of Physical Sciences, Edmonton, AB, T5J 4S2, Canada. [3]University of Alberta, Department of Earth & Atmospheric Sciences, Edmonton, AB, T6G 2E3, Canada. [4]California Institute of Technology, Division of Geological and Planetary Sciences, Pasadena, CA 91106, United States. [5]University of New Mexico, Department of Earth and Planetary Sciences, Albuquerque, NM, 87121-0001, United States.

**corresponding author. Email address: ewalton@ualberta.ca / waltone5@macewan.ca*
Keywords: Shock veins, martian meteorites, majoritic garnet, impact metamorphism, high-pressure phases, impact cratering

ABSTRACT

NWA 8159 is an augite-rich martian basalt, formed by cooling of a relatively evolved, Ca-rich, Ti-poor and LREE-depleted lava, under relatively oxidizing conditions, during the early Amazonian. In addition to its distinct igneous petrogenesis and high fO_2, NWA 8159 is also set apart from most martian shergottites with respect to the low degree of shock metamorphism required to preserve crystalline igneous plagioclase (An_{50-65}). In this study, mineral transformations within and adjacent to shock veins in NWA 8159 were investigated using scanning electron microscopy, Raman spectroscopy and transmission electron microscopy to better constrain the unusal shock history of this meteorite. The transformation of olivine to ahrensite (Fe-ringwoodite) along shock vein margins, and tissintite and coesite formed from igneous mineral (labradorite and silica) grains entrained as clasts within shock veins has been documented in this study. We report on a previously unidentified mineral assemblage of Ca-Na-majoritic garnet, sodic-clinopyroxene and stishovite crystallized from shock melt. This mineral assemblage indicates a crystallization pressure of approximately 16 GPa, which is within the range of previous shock pressure estimates for this meteorite (15–23 GPa). The presence of a majoritic garnet-bearing assemblage throughout veins up to 0.6 mm wide indicates that the sample remained at high-pressure throughout the melt vein quench. Based on thermal models, the sample must have remained at high pressure for ~100 ms. This shock duration is an order of magnitude longer than those experienced by more highly shocked shergottites such as Tissint or Zagami (>30 GPa; 10–20 ms) and would seem to imply a relatively large impact event. Recent numerical models demonstrate that a range of shock pressures and durations are realized by rocks within the ejected spall zone of a hypervelocity impact. The shock conditions experienced by NWA 8159 therefore do not require an impact event distinct from other shergottites. Rather, our findings suggest that this meteorite originated from near the martian surface at the edge of the impact site. The shock history of NWA 8159 provides a picture of Mars consistent with that

derived from remote observation; that of a random cratering process that samples a geologically long-lived and complex planet.

1. INTRODUCTION

Hypervelocity impact events deliver meteorites to Earth from the martian near-surface (Melosh, 1985). Martian meteorites originate within a "spall zone" – a zone of interference between shock waves and rarefactions near the zero-pressure free surface, leading to a large inverted pressure gradient, i.e., decreasing pressure with depth. This spall zone comprises solid rock that is accelerated to speeds sufficient to exceed the escape velocity of Mars (>5.03 km/s). The process of spallation has been studied analytically and numerically (Melosh, 1985; Warren, 1994; Melosh, 1995; Head et al., 2002; Artemieva and Ivanov, 2004). During the ejection process, the rock fragments – some destined to become meteorites – are shock metamorphosed. Resultant shock effects may manifest as deformation of host rock minerals including mosaicism, mechanical twinning and development of planar fractures in olivine and pyroxene, and / or as mineral transformation including amorphization of plagioclase to a diaplectic glass called maskelynite. All martian meteorites record shock effects and their study can be used to estimate the peak shock pressure, shock temperature, post-shock cooling history and shock pulse duration experienced by the rocks (e.g., Langenhorst and Poirier, 2000; Beck et al., 2005, Fritz and Greshake, 2009; Walton 2013, Walton et al., 2014 and references therein). During shock, shear zones develop along which small volumes of melt are generated. If the melt crystallizes at high-pressure, then the mineral assemblage that crystallizes within the shock vein may be used to constrain part of the shock-pressure history of the sample (Sharp and DeCarli, 2007). Through high-resolution numerical models, shock conditions experienced by meteorites, revealed by careful study of shock deformation and transformation effects, can be linked to the resultant crater from which they were ejected. The ability to relate martian meteorites to a specific impact crater and its source terrain will significantly increase the scientific value of these samples, because, at present, they remain the only materials available for direct study using high precision instrumentation in Earth-based labs.

Northwest Africa (NWA) 8159 was found as a single stone weighing 149.83 g, with an intergranular texture composed of augite (~48 modal%), plagioclase (~37 %), olivine (~5 %), magnetite (~5 %), maghemite (~0.5%) and minor orthopyroxene (1 vol%) (Herd et al., 2017). A Sm-Nd age of 2.37 ± 0.5 Ga, its augite-rich mineralogy, distinct bulk composition, and oxygen fugacity set NWA 8159 apart from martian shergottite meteorites, aside from recently discovered NWA 7635 (Lapen et al., 2017). However, NWA 8159 and NWA 7635 have distinctly different $\varepsilon^{182}W$ values (Kruijer et al., 2017) and do not appear to be paired. NWA 8195 is classified as a martian (augite basalt) which is defined as a martian meteorite composed of augite-rich basalt; not assigned to the shergottite, nakhlite, or chassignite types (Ruzicka et al., 2013). In addition to its igneous petrogenesis, NWA 8159 is also distinct with respect to the degree of shock metamorphism recorded in its constituent minerals; igneous plagioclase (An_{50-65}) in the bulk rock is crystalline (Herd et al., 2017). This was the first martian meteorite discovered to preserve

igneous plagioclase, however, preliminary reports of several shergottites with crystalline plagioclase have recently been documented (NWA 4480, Irving et al., 2016; NWA 10416, Walton et al., 2016a). Preservation of crystalline feldspar indicates a relatively low bulk shock pressure of ~15–23 GPa (Herd et al., 2017), in contrast to complete transformation of plagioclase to maskelynite in most shergottites, requiring shock pressures on the order of ~30–45 GPa (Fritz et al., 2005).

Our work builds off the earlier study of Herd et al. (2017), which focused on the igneous petrogenesis of NWA 8159 to assess its relationship with shergottites. The report of crystalline feldspar preserved in the host rock by Herd et al. (2017), which is rare among the current martian meteorite suite, gives merit to a thorough characterization of the shock history of this meteorite which may be deduced from the minerals associated with quenched shock melt. In this study, we employed an array of advanced analytical techniques including scanning and transmission electron microscopy and Raman spectroscopy to characterize the mineralogy associated with shock veins in NWA 8159. We report on previously unknown solid-state phase transformations in NWA 8159 and the first description of shock melt crystallization products. Thermals models and crystal-growth calculations are applied to constrain the post-shock cooling history of NWA 8159. This advances our understanding of the high-pressure, high-temperature conditions induced by a dynamic collision event on a previously unsampled portion of martian crust and constrains the size of the source crater.

2. MATERIALS AND METHODS

Two polished samples of NWA 8159 were investigated by transmitted and reflected light microscopy. A network of shock veins cuts across igneous minerals, ranging from 20 μm up to 1 mm apparent width. Detailed microtextures of transformed minerals in the host rock adjacent to, and entrained as clasts within, the shock vein as well as the shock vein matrix mineralogy, were characterized using a Zeiss EVO MA LaB6 filament scanning electron microscope (SEM) in backscattered electron (BSE) imaging mode at the University of Alberta (UAb). BSE images were acquired using a Si diode detector under conditions of 20 kV (accelerating voltage) and 7-10 mm working distance. Major and minor element abundances were measured at UAb using a JEOL 8900 electron microprobe (EMP). Analyses on olivine and ahrensite were conducted using an accelerating voltage of 15 kV and 10 nA beam current. For small micron-size garnets we employed a lower accelerating voltage (10 kV) and longer count time (120 s on peaks); at these conditions the fully focused beam size from a conventional W filament is ~100 nm. For an average garnet density of 4.0 g/cm^3 the estimated beam spread in the sample is 0.8 μm, which will vary slightly depending on the energy of the X-ray analyzed. The estimated analytical volume is therefore ~1 μm. Natural minerals were used as standards. Forsterite (Si), garnet (Al), rutile (Ti), chromite (Cr), fayalite (Fe), rhodonite (Mn), forsterite (Mg), diopside (Ca), albite (Na), sanidine (K), apatite (P), sphalerite (S) and nickel metal (Ni) were used as mineral standards for olivine and ahrensite; garnet (Si, Al, Mg), rutile (Ti), chromite (Cr), fayalite (Fe),

rhodonite (Mn), diopside (Ca), albite (Na), sanidine (K), apatite (P), sphalerite (S) and nickel metal (Ni) were used as mineral standards for garnet. Matrix, absorption, stopping power and fluorescence corrections were conducted by the ZAF procedure. The excel spreadsheet of Locock (2008) and Grew et al. (2013) was used to recast chemical analysis of garnets into end member components and to derive chemical formulas following IMA recommendations. Detection limits at the 99% confidence level are as follows: SiO_2 (0.01 wt%), Al_2O_3 (0.02 wt%), TiO_2 (0.02 wt%), Cr_2O_3 (0.03 wt%), FeO (0.02 wt%), MgO (0.02 wt%), MnO (0.02 wt%), CaO (0.01 wt%), P_2O_5 (0.02 wt%), Na_2O (0.01 wt%), NiO (0.03 wt%) and K_2O (0.02 wt%).

High-pressure minerals were identified by Raman spectroscopy using a Bruker SENTERRA micro-Raman instrument at MacEwan University. The 100X objective of a petrographic microscope was used to focus the excitation laser beam (532 nm laser) to a focal spot size of ~1 µm. A sequence of two-10 s exposures, acquired using a laser power of 10 mW, was then summed to achieve the final spectrum. Backgrounds of the spectra were graphically reduced using the OPUS v. 6.5 spectroscopy software. Four regions of interest identified in SEM images were selected for focused-ion-beam (FIB) sectioning for Transmission Electron Microscopy (TEM) analysis. FIB lift-out was performed using a FEI Nova 200 NanoLab in the LeRoy-Eyring Center for Solid Sate Science (LE-CSSS) at Arizona State University (ASU). A gallium ion beam was accelerated to 30 kV during sputtering of the slices. The FIB sections were approximately 100 nm in thickness. Analytical TEM was performed on the FIB sections using a FEI CM200-FEG and an FEI Techni 200-FEG in the LE-CSSS at ASU. Energy Dispersive X-ray (EDX) analyses were performed with an EMiSpec analytical system on the CM200. TEM EDX-determined wt% oxide abundances were normalized to 100. Analyses were quantified with the EMiSpec system using system generated Cliff-Lorimer k factors. No absorption or fluorescence corrections were applied. Nanometer scale mineralogy was determined using a combination of imaging, selected area electron diffraction (SAED), convergent beam electron diffraction (CBED) and EDX analysis.

Numerical methods were employed to model the shock vein cooling history to constrain shock duration or dwell time, defined as the time that elapses between the arrival of the shock front and that of the release or rarefaction wave. For a shock vein that crystallizes at high-pressure, the time required for the vein to reach the solidus provides a minimum estimate of the amount of time that the sample remained at high pressure, and therefore a minimum estimate of shock duration (Xie et al., 2006; Shaw and Walton, 2013; Sharp et al., 2015) We used a finite element heat transfer (FEHT) code to calculate cooling histories of shock melt and the surrounding host rock as a function of starting temperature and vein thickness. It should be noted that vein width (600 μm) is measured in the two dimensions of the thin section and is therefore an apparent width. The 1-D simulation is set in the Cartesian coordinates to represent heat conduction from planar 3-D melt. The FEHT software has specific setup for cylindrical problem that were not applied to our models.

3. RESULTS

3.1 Shock effects in the igneous host rock

The igneous texture of the studied samples is intergranular, comprising plagioclase, augite, olivine, orthopyroxene and magnetite, with a grain size generally between 100–200 μm (**Fig. 1**). Olivine and pyroxene in the host rock exhibit irregular fractures and extinction varies from undulose to weak mosaicism. Planar fractures are developed in olivine, with up to 3 sets of closely spaced (1–5 μm) fractures with distinct orientations observed in a single grain. Polysynthetic mechanical twin lamellae, attributed to shock, are present in some pyroxene grains. Consistent with previous reports (Herd et al., 2017), plagioclase in the host rock, far from regions of local shock melting, is anisotropic (crystalline) with typical albite polysynthetic twinning and cleavage characteristic of igneous plagioclase.

3.2 Mineral transformations associated with shock veins

The igneous texture is cut across and displaced by a network of opaque shock veins containing entrained mineral and lithic fragments (**Fig. 2**). At the shock vein margin, olivine is partially transformed to ahrensite (Fe_2SiO_4-rich ringwoodite; Ma et al., 2016a). EMP WDS analyses show this phase to be enriched in iron ($Fa_{73.1\text{-}74.5}$) compared to adjacent olivine ($Fa_{66.6\text{-}67.1}$) (**Table 1**). This compositional difference between olivine and ahrensite is observed as a difference in brightness in BSE imaging mode (**Fig. 2b**). Ahrensite was confirmed by peak positions in the Raman spectrum – igneous olivine shows sharp peaks at 816 cm^{-1} and 841 cm^{-1}, characteristic of crystalline olivine (**Fig. 3**). These peaks positions are distinct from those of ahrensite at 672 cm^{-1}, 782 cm^{-1} and 841 cm^{-1} **(Fig. 3),** and are due to antisymmetric (T_{2g}) and symmetric (A_{1g}) stretching vibrations of the isolated SiO_4 tetrahedra (Chopelas et al., 1994). The Raman spectrum of ahrensite contains additional broad, high amplitude peaks at 118 cm^{-1} and 202 cm^{-1}.

Plagioclase transformation, like olivine, is restricted to areas where former igneous grains are in contact with the now crystallized shock melt (**Fig. 2c**). Within a zone ~20–300 μm distant from shock veins, plagioclase forms smooth and unfractured amorphous grains which preserve the original grain boundaries of the igneous precursor. Within a thin zone (10–40 μm) in direct contact with the shock vein margin, amorphous plagioclase has transformed to tissintite (**Fig. 2c**), a shock-induced pyroxene with plagioclase composition, $(Ca,Na,\square)AlSi_2O_6$, first discovered in the depleted picritic shergottite Tissint (Ma et al., 2015). In addition to this tissintite occurrence, identical to that reported by Herd et al. (2017), we note two previously unidentified occurrences of tissintite in NWA 8159: 1) as rounded clasts of transformed plagioclase (formerly single crystals) entrained within the shock vein (**Fig. 2d**), and 2) within lithic basaltic clasts entrained within the shock vein containing plagioclase and silica-rich igneous mesostasis. Raman spectra acquired from these latter regions are consistent with a mixture of coesite (520 cm^{-1})

formed from mesostasis silica and tissintite (690 and 1100 cm^{-1}) formed from plagioclase (**Fig. 3**).

3.3 Mineralogy and composition of the shock vein matrix

The shock vein matrix has a granular texture with fine-grained margins and increasing crystal size toward vein centers. BSE images show the dominant silicate phase forms large poikilitic grains. In the vein center these poikilitic grains are accompanied by blocky silicate crystals and small bright spheres (**Fig. 4**). Raman spectra, collected as single spot analyses on several individual areas of the shock vein, suggest an intimate mixture of several phases including garnet + pyroxene + coesite + Fe-sulfide (**Fig. 3**). Coesite was distinguished by a high amplitude peak at ~525 cm^{-1} (Gillet et al., 1990), whereas garnet was identified by two peaks centered over 664 cm^{-1} and 910 cm^{-1} (Rauch et al., 1996), and pyroxene by a characteristic doublet near 662 cm^{-1} and 1008 cm^{-1} (Wang et al., 2001). EMP analyses of the largest granular grains to crystallize within the vein show that they are almandine-rich garnet with an average general formula $(Fe_{1.661}Ca_{0.788}Na_{0.262}Mg_{0.229}Mn_{0.036})_{\sum 2.976}(Al_{1.167}Si_{0.538}Mg_{0.259}Ti_{0.03}Cr_{0.007})_{\sum 2.001}Si_3O_{12}$ (Table 1). The sodium content of these crystals ranges from 1.27─2.28 wt% Na_2O. Excess silicon, 0.538 per formula unit, corresponds to a 54% majoritic component (Grew et al., 2013).

3.2 Transmission electron microscopy

Four FIB sections were acquired from areas within and adjacent to NWA 8159 shock veins (**Fig. 4**). FIB 1 was extracted from ahrensite into the fine-grained margin of the shock vein (Fig. 5). FIBs 2 and 3 were taken in the center of a wider portion of the vein; FIB 2 targeted two large poikilitic garnet grains (Fig. 6) and FIB 3 sampled larger poikilitic crystals and smaller blocky grains (**Fig. 7**). FIB 4 was extracted as a transect from olivine through a bright rim consisting of light and dark areas in BSE images (**Fig. 8e**). TEM bright field images and SAED patterns collected from FIB 1 confirm the formation of ahrensite from olivine in those grains in direct contact with now-crystallized shock melt (**Fig. 2b, 5a**). The shock vein margin is composed of a mixture of majoritic garnet and stishovite as the dominant mineral assemblage within the fine-grained vein edge (**Fig. 5b-d**). Garnets range from 200-nm equant crystals to 1-μm poikilitic crystals. The average chemical formula for these majoritic garnets from TEM EDX measurement is $(Fe_{1.64}Ca_{0.83}Na_{0.34}Mg_{0.15}Mn_{0.04})(Al_{1.31}Si_{0.38}Mg_{0.27}Ti_{0.04})Si_3O_{12}$; they are Na-rich almandine-grossular garnets with ~38% majoritic component. Stishovite occurs as tetragonal prisms around smaller garnets (**Fig. 5a-c**). The average formula for the stishovite from TEM EDX is $Si_{0.96}Al_{0.04}Fe_{0.01}O_2$. FIB sections across the central region of a 0.6-mm thick shock vein (FIBs 2 and 3) show different assemblage from that observed at the fine-grained margin, comprising majoritic garnet, clinopyroxene, stishovite and silicate glass, along with Fe-sulfide (**Fig. 7**). The garnets are also poikilitic, like those observed in FIB 1 (Fig. 5d) at the shock vein margin, with abundant silicate glass (amorphous) and rod-shaped stishovite inclusions (**Fig. 6; Fig. 7a, b**). Diffuse rings

in SAED patterns identified amorphous inclusions, while stishovite was identified based on morphology and indexed convergent-beam electron diffraction (CBED) patterns (**Fig. 5b, 7b**). Semi-quantitative TEM EDX analyses acquired on these garnets indicate they are Na-rich almandine-grossular garnets with ~36% majoritic component: $(Fe_{1.54}Ca_{0.90}Na_{0.36}Mg_{0.26}Mn_{0.04})(Al_{1.30}Mg_{0.36}Si_{0.36})Si_3O_{12}$. This chemical composition is close to that obtained by EMP analysis; both showing excess silicon and significant amounts of sodium (**Table 1**). The pyroxene was identified as a solid solution between jadeite and hedenbergite with an average chemical formula: $(Na_{0.43}Ca_{0.32}Fe_{0.25})(Fe_{0.51}Mg_{0.16}Al_{0.33})Si_{2.03}O_6$, based on EDX analyses. EDX on stishovite crystals show they are nearly pure SiO_2, with trace Fe (0.04 atoms per formula unit, apfu) and Al (0.04 apfu). FIB 4 reveal the bright rim surrounding olivine to be composed of magnetite and clinoenstatite (**Fig. 8a-d**), consistent with peaks in the Raman spectrum acquired from this region (**Fig. 3**).

4. DISCUSSION

4.1 Shock effects in the bulk rock

Shock deformation in non-shock veined regions of the host rock is consistent with low to moderate degrees of shock metamorphism, estimated to be ~15–23 GPa by Herd et al. (2017). This shock pressure estimate was based on shock deformation in olivine (mosaicism, planar fractures) and pyroxene (mosaicism, mechanical twinning), and the partial transformation of plagioclase (An_{50-65}) to maskelynite. Our results on shock deformation in the bulk rock agree with low levels of shock experienced by NWA 8159. In our study, the Raman spectrum from olivine shows sharp peaks characteristic of well-crystalline material (**Fig. 3**). Additional features in the Raman spectrum documented from olivine in strongly shocked martian meteorites NWA 2737 and NWA 1950 (van de Moortèle et al., 2007), are notably absent in NWA 8159. We have not observed broadening of peaks, characteristic of highly disordered olivine crystals, or the presence a weak peak at 760 cm^{-1}, characteristic of defects. Similarly, we see no additional broad bands at 650 and 686 cm^{-1} to suggest the presence of the shock-produced ζ-$(Mg,Fe)_2SiO_4$ olivine polymorph (van de Moortèle et al., 2007).

4.4 Localized mineral transformations

In NWA 8195, plagioclase transformation, like the ahrensite formed from olivine, is associated with shock veins. A transition from crystalline igneous plagioclase to maskelynite and finally tissintite is observed within the host rock, as the margin of the shock vein is approached (**Fig. 2c**). The coexistence of crystalline plagioclase and maskelynite, a shock-produced diaplectic glass of plagioclase composition, in NWA 8195 is rare amongst most other martian basalts where igneous plagioclase has been completely transformed to diaplectic glasses or

normal vesiculated glass (Fritz et al., 2005). Here, we explore how these transformations constrain the shock pressure experienced by NWA 8159. Partial transformation of labradoritic plagioclase to maskelynite at elevated temperature requires shock pressure 15─20 GPa (Daniel et al., 1997; Kubo et al., 2009). The localized transformation of olivine to ahrensite at shock vein margins was confirmed by peak positions in the Raman spectrum (**Fig. 3**). Strong low frequency peaks near 118 cm^{-1} and 202 cm^{-1} may be associated with localized modes generated by Fe substitution (Fe^{2+}, Fe^{3+}), which explains their absence in pure Mg_2SiO_4-ringwoodite (Kleppe et al., 2002). Composition determined from electron microprobe spot analyses on ahrensite and adjacent olivine show that ahrensite is richer in iron. This same iron-enrichment has been noted for high-pressure olivine polymorphs in other meteorites (e.g., Ohtani et al., 2004; Walton, 2013) and attributed to Fe-Mg exchange during transformation and therefore diffusion-controlled growth. Diffusion kinetics are enhanced by high temperatures, small grain sizes, high strain rates and numerous defect sites within highly deformed minerals. The transformation of fayalitic olivine (Fa_{75}) to ahrensite does not provide tight constraints on the shock pressure, because the transformation can occur under any conditions where anhensite has a lower free energy than Fa_{75}-olivine. Based on the phase diagram for 1600°C (Fei and Bertka, 1991), the olivine-ahrensite transformation indicates a minimum pressure of ~10 GPa (**Fig. 10a**). Above 18 GPa, magnesiowüstite plus stishovite are stable relative to ahrensite, but this may not provide an upper bound on pressure because the diffusion controlled reaction to magnesiowüstite plus stishovite is kinetically inhibited, except at very high temperatures. Ahrensite found in Tissint (Ma et al. 2016) indicate that it can persist to pressures estimated to be 19 to 30 GPa (Walton et al, 2014). The presence of ahrensite is consistent with shock pressure estimates from the partial transformation of plagioclase (An_{50-65}) to maskelynite (~15–23 GPa; this study, Herd et al., 2017).

FIB 4 targeted a bright rim (in BSE images) mantling olivine adjacent to the shock vein. Similar textures described from the Tissint shergottite were shown by TEM to represent the breakdown of olivine to bridgmanite and magnesiowüstite (**Fig. 8e**) (Walton et al. 2014). However, the olivine rim in NWA 8159 is composed of low-Ca pyroxene (clinoenstatite) + magnetite, the former corresponding to darker areas in BSE images and the latter to bright grains. This assemblage and texture is identical to a pyroxene + magnetite symplectic intergrowth described by Herd et al. (2017) and attributed to subsolidus reaction of olivine under fO_2 condition slightly above QFM. Therefore, this intergrowth is attributable to an igneous process but not to shock.

Offset and displacement of igneous minerals along shock vein margins indicates a shear and friction-induced mechanism for their origin and growth (**Fig. 2**). Shock veins represent local hot spots (2000─2500 ^oC) compared to the host rock where the temperature increase by shock compression is limited to a few hundred degrees (Sharp and DeCarli, 2006). Shock veins, once formed, cool by conduction of heat to the surrounding host rock (Shaw and Walton, 2013). The spatial distribution therefore reflects temperature variations within the rock and demonstrates that plagioclase transformation depends not only on the shock pressure but also on the amount of

heat available to drive phase transformations. The non-hydrostatic stress condition experienced by minerals along shock vein margins is also likely a factor driving phase transformation (Daniel et al., 1997). This association between high-pressure, high-temperature phases and shock veins is well documented from chondritic and achondritic meteorites (e.g. Langenhorst and Poirier, 2000; Sharp and DeCarli, 2006; Walton et al., 2014; Walton and McCarthy, 2017), and rocks from terrestrial impact structures (Stähle et al., 2011).

4.3 Shock vein crystallization products and constraints on pressure

NWA 8159 contains several mm-thick shock veins that have crystallized to a fine-grained granular mixture of silicate and minor sulfide. Raman spectra collected from the vein matrix (**Fig. 3**) and SAED patterns collected from two TEM FIB sections (**Fig. 4**) confirm that garnet is the dominant mineral to have crystallized from the shock melt. These equant, euhedral 1–2 μm size garnet grains form under conditions of very rapid quench and therefore rapid crystal growth rates. These growth rates, and resulting textures, are quite different from those seen in equilibrated high-pressure experiments, but are texturally similar to the quenched liquids in multi-anvil experiments (e.g., Trønnes and Frost, 2002). However, the garnets in the natural sample crystallized in a melt under rapidly decreasing temperature and therefore formed far from equilibrium, resulting in a large ΔG of reaction to drive garnet growth. The growth of laboratory-produced equilibrated garnets therefore cannot be compared to those in a natural shock vein. We consider the quench rate of the shock vein in NWA 8159 in section 4.4.

The composition of garnet was constrained using EMP wavelength dispersive spectrometry (WDS) and TEM energy dispersive X-ray spectrometry (EDX) analysis techniques. The advantage of the TEM EDX analyses over the more quantitative EMP WDS analyses is that the small spot size of the TEM, combined with the thin-film sample geometry, results in a very small excitation volume, limiting any spurious X-rays from inclusions. The calculated formulas from both methods are slightly different owing to the larger sampling volume using wavelength dispersive spectrometry; however, both EDX and WDS analyses indicate that these almandine garnets have a significant majoritic component (36–54%) and contain sodium (0.34─0.37 atoms Na per formula unit). Sodium-enriched garnets (wt% oxide) have been reported in high-pressure experiments (e.g., Ringwood and Major, 1971; Gasparik, 1989) and natural occurrences (e.g., Schertle et al., 1991). Likewise, excess silicon in garnet, up to 0.54 Si cations per $X_3Y_2Z_3O_{12}$ formula unit, is accommodated within octahedral sites, similar to Si^{4+} in stishovite, at high pressure (Ringwood and Major, 1971; Smith and Mason, 1970). The composition of these garnets crystallized from shock melts in NWA 8159 therefore indicates melt crystallization at high pressure. The first occurrence of high-pressure almandine has been reported by Ma and Tschauner (2016) in the Shergotty martian meteorite, where it crystallized with stishovite in a shock melt pocket.

The shock-vein assemblages also provide constraints on the shock pressure when combined with experimental high-pressure melting relations (Chen et al., 1996; Sharp and DeCarli, 2006).

The shock-vein margins have an assemblage of majoritic-garnet plus stishovite (**Fig. 5b-d**), whereas the vein centers have an assemblage of majoritic-garnet + clinopyroxene + stishovite (**Fig. 2d, Fig. 7**). The Na^{+} content of the clinopyroxene is charge balanced by 0.33 pfu Al^{3+} and 0.10 pfu Fe^{3+} (aegirine). This aegirine component is consistent with high-pressure crystallization. Based on the phase relations for MORB at 2300 K (Hirose et al., 1998), majorite + stishovite at the shock vein margin implies a starting crystallization pressure between 16 and 22 GPa, while the majoritic garnet + pyroxene + stishovite assemblage defining the vein center implies P <16 GPa (**Fig. 10b**). This pressure difference can be reconciled by considering quench rates. The margin quenches rapidly by conduction of heat to the colder host rock, preserving the early history of vein crystallization. The vein center quenches more slowly and records the crystallization later in the shock pulse. Therefore, we infer that the peak shock pressure was >16 GPa when the vein edge crystallized and it dropped to below 16 GPa during the 100 ms between vein edge and center crystallization (**Fig. 9**).

The melt-crystallization pressure matches well with the shock pressure required for partial amorphization of labradorite-composition plagioclase (15─23 GPa; Herd et al., 2017; this study) and with formation of ahrensite from olivine at shock vein margins (up to 18 GPa; Fig. 10a). This shock pressure estimate is lower than those of most other martian basalts (shergottites) such as Zagami (30 GPa; Langenhorst and Poirier, 2000), Shergotty (29 GPa; Stöffler et al., 1986), Dar al Gani 476 (40─45 GPa; Fritz et al., 2005), NWA 4797 (>45 GPa; Walton et al., 2012) and Tissint (>19 GPa, <30 GPa; Walton et al., 2014), in which the shock pressure has been estimated by the complete transformation of labradoritic plagioclase to maskelynite. A shock pressure estimate of ~16 GPa, based on shock vein crystallization assemblages in this study, is consistent with the preservation of crystalline plagioclase in NWA 8159 (Fritz et al., 2005).

4.4 Thermal modeling of shock vein quench time: constraints on shock duration

In NWA 8159, the crystallization of majoritic garnet throughout a 600-μm wide shock vein is evidence that the melt crystallized during the shock pulse and suggests a relatively long shock pulse duration and rapid quench of the shock melt. To model the shock vein cooling history as a function of starting temperature and vein thickness, and to constrain the shock pulse duration experienced by NWA 8159, we have employed a finite element heat transfer (FEHT) code.

In our one-dimensional model, a shock vein of 600 μm thickness is enclosed in 9 mm of host rock, with 4.5 mm on each side. A shock pressure of 16 GPa is assumed for NWA 8159, which is within the range of estimates (15–23 GPa) based on plagioclase by Herd et al. (2017). The starting temperature of the melt is 2500 K, constrained by the liquidus temperature of 2400 K for mid-ocean ridge basalt (MORB) at 16 GPa (Hirose et al., 1999). The bulk temperature of the host rock, 600 K, is the temperature for a 16 GPa shock pressure on the Hugoniot of Kinosaki basalt, appropriate for an analogue of NWA 8159 (~5% porosity; Nakazawa et al., 1997; Sekine et al., 2008). The technique for calculating the shock temperature by integration along the Hugoniot is introduced in McQueen (1989) and Gillet and El Goresy (2013).

For the modeling, the finite element heat transfer (FEHT) software was employed to calculate transient heat flow from the shock vein to the surrounding igneous host rock. The governing equation of the finite element analysis is:

$$\frac{\partial}{\partial x}\left(k\frac{\partial T}{\partial x}\right)+\frac{\partial}{\partial y}\left(k\frac{\partial T}{\partial y}\right)-\rho c\frac{\partial T}{\partial t}=0$$

where x and y are distance in two dimensions, T is temperature [K], k is thermal conductivity [$Wm^{-1}K^{-1}$], ρ is density [kgm^{-3}], c is heat capacity [$kJkg^{-1}K^{-1}$] and t is time [s]. The density of basalt at 16 GPa from static and shock experiments is consistently around 3500 kg/m^3. The isobaric heat capacity, C_P, of basalt is extrapolated to the high-pressure solidus temperature from low-pressure data (Boufihd et al., 2007; Miao et al., 2014). The values of C_P are 730 to 1400 J/kg·K for 300 to 2300 K. The latent heat and heat capacity for basaltic melt is 658 kJ/kg and 1600 J/kg·K, from melting calorimetry experiments (Lange et al., 1994). The latent heat is uniformly distributed between the solidus (2300 K) and liquidus (2400 K) temperatures in our model. The bulk composition of NWA 8159 is 10 wt% richer in FeO than representative terrestrial basalt (Herd et al. 2017), leading to slight overestimate of the heat capacity (Lange and Navrotsky, 1992). The high-pressure effect also introduces uncertainties in the heat capacity. Limited data on olivine and diopside suggest that the pressure derivative $\partial C_P/\partial P$ is approximately in the range of -1 to -3 J/kg·K·GPa (Osako et al., 2004; Wang et al., 2014). Therefore, we infer that the heat capacity of basalt at 16 GPa shock pressure is less than 5% percent different from the experimental data we used. The thermal conductivity, however, changes significantly with pressure because of the compression of the material. At ambient pressure, the thermal conductivity of basalt for 300 to 1200 K is in the range of 2.4 to 1.5 W/m·K. Although mafic minerals in NWA 8159, such as olivine, generally have higher thermal conductivity (Hofmeister et al., 1999; Osako et al., 2004), the number for basaltic rock is mostly constrained by calcic plagioclase (Clauser and Huenges, 1995). The pressure effect on thermal conductivity is commonly fitted to an exponential function $k(P,T)=k(1\ \text{Bar},T)\cdot e^{aP}$, where P is pressure in GPa and a is a fitting factor. The factor a for rock-forming minerals are in the range of 0.01 to 0.1 (Hofmeister et al., 1999; Osako et al. 2004). Since the data for plagioclase is not available, we used 0.03 of calcic pyroxene as the best approximation for factor a (Wang et al. 2014). As a consequence, the calculated high-pressure thermal conductivity for basalt and melt is 4.1 to 2.3 W/m·K.

Our heat transfer model indicates that the center of the 0.6 mm thick shock melt vein quenches to the high-pressure solidus (2300 K) in ~100 ms after the vein formation (**Fig. 9**). The crystallization of majoritic garnet throughout the melt vein, requires that the pressure remained high for the entire 100 ms solidification time, which provides a constraint for the duration of the shock pulse. Based on the crystallization assemblage, the edge (within 20 μm from the melt-host boundary) of the vein, consisting of majoritic garnet plus stishovite, may have a higher crystallization pressure than the vein interior with additional clinopyroxene. Since the boundary solidifies within 10 ms (**Fig. 9**), it appears that the shock pressure slightly decreased between 10

and 100 ms. Heat transfer in our model is based on conduction through both melt and surrounding host rock, although turbulence in the shock melt would enhance heat transfer within the melt (Tschauner et al., 2009). Turbulence is likely in shock veins that contain materials with significantly different shock impedance and particle velocities, such as immiscible silicate and metal-sulfide melts. Because the shock melt vein of NWA 8159 is predominantly silicate, with very little sulfide (**Fig. 2**), we conclude that the shock-induced turbulence is unlikely to be a major factor in transferring heat out of the shock melt in NWA 8159. The heat content of the shock melt and the efficiency of heat transfer are the most important factors for determining melt quench rates. The high-pressure melt has much higher energy density than the host rock, making the volume of melt and melt/host ratio the predominant factors for the cooling history of the melt-vein center (Hu and Sharp 2017). Even if turbulence enhances heat transfer within the melt, heat transfer through the solid host is the bottleneck for dissipating melt-vein heat.

Host rock near the edge of the shock vein is significantly heated by conduction from adjacent shock melt. Mineral grains in the host rock within a distance of 5 μm from the vein margin can reach temperatures 1700 K. This is in contrast to minerals more distant from the vein margin (50 μm) where temperatures are significantly lower, on the order of 1400 K. This zone of host rock near the edge of shock vein that is heated by conduction from the shock vein corresponds to the same zone in which the transformation of plagioclase to maskelynite and tissintite, and olivine to ahrensite is documented (**Fig. 2**). Our model shows that the peak temperature of the host is a function of its distance to the shock melt boundary. Within 5 μm from the melt vein, the host mineral grains can reach 1700 K (**Fig. 9**) and experience rapid transformation to their high-pressure polymorphs (**Fig. 2**). For host rock 50 μm from the melt, the 1400 K peak temperature (**Fig. 9**) is not sufficient to enable reconstructive transformation within the 100 ms high-pressure pulse (e.g. Kerschhofer et al., 2000; Xie and Sharp, 2007). This association between the quenched products of shock-melting and high-pressure minerals has been well-documented from meteorites and terrestrial impact structures (this study; Xie and Sharp, 2007; Walton et al., 2014; Ma et al., 2016b; Walton et al. 2016b). Nevertheless, the 1000–1400 K peak temperature experienced by the host rock in this zone still enhances the amorphization of plagioclase (Kubo et al. 2010), though the latter transformation may also be governed by shear stresses experienced by host rock minerals along the shock vein margin, in addition to elevated temperature and pressure (Daniel et al. 1997).

4.5 Shock duration estimates from garnet and ahrensite growth rates

The grain sizes and growth rates of high-pressure minerals provide supportive constraints for estimating shock duration (Xie and Sharp, 2007; Ma et al., 2016). Ma et al. (2016) calculated the correlations between shock pulse, grain size and temperature for ahrensite transformation in Tissint, using the grain-growth kinetic data for the olivine-ringwoodite transformation (Liu et al., 1998; Kerschhofer et al., 2000). TEM investigation indicates the grain size of ahrensite adjacent to the melt vein in NWA 8159 is up to 300 nm (Fig. 5), indicating up to 150 nm of grain growth during shock. Using the grain size analysis of Ma et al. (2016), 150 nm of grain growth in 100

ms requires a temperature of approximately 1550 K. This is consistent with the observation that ahrensite transformation only occur in host rock at distance less than 50 μm from the melt (Fig. 2) and with our thermal models (Fig. 9). A distance of 50 μm from the melt vein is where the peak temperature in the host rock remains below 1400 K (Fig. 9). At greater distance from the melt, the peak temperature is too low to enable the high-pressure transformation.

4.6 NWA 8159 impact history

The shock pulse duration of martian meteorites has been estimated using different approaches including ringwoodite-growth kinetics, diffusion and shock-melt quench to be ~10 ms (Beck et al., 2005), ~10 ms (Fritz and Greshake, 2009), ~1 s (Baziotis et al., 2013), ~10─20 ms (Walton et al., 2014) and ~1–10 ms (Ma et al., 2016a). The large ringwoodite grains observed by Baziotis et al., (2013), used to infer a long (1 s) shock pulse duration for Tissint, were later shown by TEM, electron back-scattered diffraction and BSE imaging to be polycrystalline (Walton et al., 2014; Ma et al., 2016a). Therefore, this long shock duration (1 s) can be disregarded, and the shock pulse duration for martian meteorites is on the order of 1─20 ms. A shock pulse duration of 100 ms for NWA 8159 is therefore an order of magnitude longer than that of other shergottites. This observation, coupled with the preservation of crystalline plagioclase in NWA 8159, calls for a unique impact scenario for NWA 8159 compared to the current collection of martian basalts. High spatial resolution numerical models of meteorite-producing impact events on Mars have shown that the pressure experienced by target rocks and shock duration, τ, depends not only on impactor size, but also on the location of the sample relative to the impact site (Bowling et al., 2015). Lines of equal pressure and lines of equal shock duration have different spatial orientations, therefore rocks subjected to a given shock pressure can experience different shock durations. For a 10-km impactor, near-surface rocks subjected to the peak pressures estimated for NWA 8159 in this study and by Herd et al. 2017 (15–20 GPa) experience dwell times of 1─2 seconds, an order of magnitude longer than our estimate of shock duration. In contrast, a 1 km impactor can eject rocks at moderate shock pressure (15─20 GPa) that experience a shock duration of 100 ms. This latter scenario accounts for the shock conditions experienced by NWA 8159.

The ejection age of NWA 8159, calculated from the sum of its cosmic ray exposure age and terrestrial age, is 1.2 ± 0.1 Ma (Herd et al., 2017). This ejection age is, within error, in the range of those from other shergottites, notably that of the Tissint meteorite fall, with a CRE age from ^{3}He, ^{21}Ne and ^{38}Ar of 1.2± 0.4, 0.6 ± 0.2 and 0.9 ± 0.4 Ma, respectively (Chennaoui Aoudjehane et al., 2012). This suggests that NWA 8159 may belong to a group of ~12 depleted shergottites having an ejection age of ~1.1 Ma (Wieler et al., 2016; Lapen et al., 2017). The higher shock pressures (>20 GPa) and shorter shock duration (~10–20 ms) experienced by other shergottites suggest that they originated closer to the point of impact, but do not require appreciably different ejection conditions than NWA 8159. Therefore, all of these samples were possibly ejected during a single impact event, but from appreciably different locations relative to the point of impact. This is consistent with the distinct petrography and age of NWA 8159.

5. SUMMARY AND CONCLUSIONS

Augite basaltic shergottite NWA 8159 is a ~2.37 Ga sample of the martian Amazonian crust. In addition to a distinct age and igneous petrogenesis, this meteorite also exhibits a unique shock history, characterized by low levels of shock preserving crystalline igneous plagioclase. Detailed characterization of mineral transformation within and adjacent to localized small volumes of shock melt have been conducted as part of this study using Raman spectroscopy and transmission electron microscopy. We report a new occurrence of tissintite as former plagioclase entrained as mineral clasts within shock veins as well as coesite. Fayalite-rich olivine in direct contact with shock melt has been transformed to ahrensite (Fe-ringwoodite) at pressures ~10–18 GPa. Within the shock vein, an assemblage of majoritic garnet + stishovite has crystallized from rapidly quenched vein margins. The center of thicker shock veins, up to 0.6 mm width, exhibit a distinct assemblage of majoritic garnet + stishovite + clinopyroxene. Based on these assemblages a peak shock pressure of 16–18 GPa is estimated for crystallization of the shock vein. Thermal conduction models constrain the duration of high-pressure crystallization to have been ~100 ms; compared to other shergottites with shock duration on the order of 10–20 ms. Numerical models of impact ejection from Mars show this relatively long shock duration and modest shock pressure are consistent with ejection from a single impact event with other highly-shocked shergottites, albeit from different locations from the point of impact. Strongly shocked shergottites (>30 GPa) that experience a short shock duration (10–20 ms) original closer to the point of impact compared to NWA 8159.

Acknowledgements. We thank Andrew Locock and Martin von Dollen at the University of Alberta for expertise in EMP and sample preparation, respectively. Financial support for this project was provided by NSERC Discovery Grant RES00007057 awarded to ELW and NASA Cosmochemistry Grant NNH08ZDA001B-Cos awarded to TGS. The authors would like to thank three anonymous reviewers who provided input that improved the overall quality of this manuscript. We acknowledge the use of facilities within the Eyring Materials Center at Arizona State University supported in part by NNCI-ECCS-1542160.

References

Artemieva N. and Ivanov B. (2004) Launch of martian meteorites in oblique impacts. *Icarus* **171**, 84–101.

Beck P., Gillet P., El Goresy A. and Mostefaoui S. (2005) Timescales of shock processes in the solar system from mineralogical transformations in chondrites and martian meteorites. *Nature* **435**, 1071–1074.

Bläß U.W. (2013) Shock-induced formation mechanism of seifertite in shergottites. *Physics and Chemistry of Minerals* 40, 425-437.

Bouhifd M. A., Besson P., Courtial P., Gérardin C., Navrotsky A. and Richet P. (2007) Thermochemistry and melting properties of basalt. *Contrib. Mineral. Petrol.* **153**, 689–698.

Bowling T. J., Johnson B. C. and Melosh H. J. (2015) Simulating dwell times at high pressure and temperature following an impact: relating thin section to source crater. *Lunar Planet Sci XLVI*. Lunar Planet Inst., Houston. #2289 (abstr.).

Chen M., Sharp T. G., El Goresy A., Wopenka B. and Xie X. (1996) The majorite-pyrope + magnesiowüstite assemblage: Constraints on the history of shock veins in chondrites. *Science* **271**, 1570–1573.

Chopelas A., Boehler R. and Ko T. (1994) Thermodynamics and behaviour of ϒ-Mg_2SiO_4 at high pressure: implications for Mg_2SiO_4 phase equilibrium. *Phys. Chem. Miner*. **21**, 351–359. Doi: 10.1007/BF00203293.

Clauser C. and Huenges E. (1995) Thermal Conductivity of Rocks and Minerals. In *Rock Physics & Phase Relations* (ed. T. J. Ahrens). American Geophysical Union. pp. 105–126.

Daniel I., Gillet P., McMillan P. F., Wolf G. and Verhelst M. A. (1997) High-pressure behavior of anorthite: Compression and amorphization. *J. Geophys. Res*. **102**, 10,313–10,325.

Enami M., Cong B., Yoshida T. and Kawake I. (1995) A mechanism for Na incorporation in garnet: An example from garnet in orthogneiss from the Su-Lu terrane, eastern China. *Am. Miner*. 80, 475–482.

Fritz J., Artemieva N. A. and Greshake A. (2005) Ejection of martian meteorites. *Meteor. Planet. Sci*. **40**, 1393–1411.

Fritz J. and Greshake A. (2009) High-pressure phases in an ultramafic rock from Mars. *Earth Planet. Sci. Lett*. **288**, 619–623.

Gillet P. and El Goresy A. (2013) Shock Events in the Solar System: The Message from Minerals in Terrestrial Planets and Asteroids. *Ann. Rev. Earth Planet. Sci.* **41**, 257–285.

Gillet P., Le Cleach A. and Madon M. (1990) Pressure dependence of Raman spectra of SiO_2 polymorphs: alpha-quartz, coesite and stishovite. In High-pressure research in mineral physics (Eds. M. H. Manghnani and Y. Syono). Terra Scientific Publishing Company (Tokyo) and the American Geophysical Union (Washington, D. C.), pp. 347–360.

Greshake A., Fritz J. and Stöffler D. (2004) Shock metamorphism of the olivine-phyric shergottite Yamato 980459: Evidence for a two-stage cooling and a single-stage ejection history. *Geochim. Cosmochim. Acta* **68**, 2359–2377.

Grew E. S., Locock A. J., Mills S. J., Galuskina I. O., Galuskin E. V. and Hålenius U. (2013) IMA report. Nomenclature of the garnet supergroup. *American Mineralogist* **98**, 785–811.

Head J. N., Melosh H. J. and Ivanov B. A. 2002. Martian meteorite launch: high speed ejecta from small craters. *Science* **298**, 1752–1756. Doi:10.1126/science.1077483.

Herd C. D. K., Walton E. L., Agee C. B., Muttik N., Zeigler K., Shearer C. K., Bell A. S., Santos A. R., Burger P. V., Simon J. I., Tappa M. J., McCubbin F. M., Gattacceca J., Lagroix F., Sanborn M., Yin Q. –Z., Cassata W. S., Borg L. E., Lindvall R. E., Kruijer T. S., Brennacka G. A., Kleine Th., Nishiizumi K., and Caffee M. W. (2017). The Northwest Africa 8159 martian meteorite: Expanding the martian sample suite to the early Amazonian. *Geochim. Cosmochim. Acta*. **218**, 1–26.

Hirose K., Fei Y., Ma Y. and Mao H.-K. (1999) The fate of subducted basaltic crust in the Earth's lower mantle. *Nature* **397**, 53–56.

Hofmeister A. M. (1999) Mantle Values of Thermal Conductivity and the Geotherm from Phonon Lifetimes. *Science* **283**, 1699–1706.

Humayun M., Nemchin A., Zanda B., Hewins R.H., Grange M., Kennedy A., Lorand J.-P., Göpel C., Pont S. and Deldicque D. (2013) Origin and age of the earliest martian crust from meteorite NWA 7533. *Nature*, doi: 10.1038/nature12764.

Irving A. J., Andreason R., Righter M., Lapen T. J., Busemann H., Izawa M., Moser D. E. and Sipiera P. P. (2016) Northwest Africa 4480 revisited: Petrologic, isotopic, and noble gas studies of an unshocked, maskelynite-free mafic shergottites with a long cosmic ray exposure age. 47th Lunar and Planetary Science Conference, Abstract #2330.

Kerschhofer L., Rubie D. C., Sharp T. G., McConnell J. D. C. and Dupas-Bruzek C. (2000) Kinetics of intracrystalline olivine–ringwoodite transformation. *Phys. Earth Planet. Inter.* **121**, 59–76.

Kleppe A., Jephcoat A.P., Smyth J.R. and Frost F.J. (2002) On protons, iron and the high-pressure behaviour of ringwoodite. *Geophys. Res. Lett.* **29**, 171–174. doi: 10.1029/2002GL015276.

Kubo T., Kimura M., Kato T., Nishi M., Tominaga A., Kikegawa T. and Funakoshi K. (2010) Plagioclase breakdown as an indicator for shock conditions of meteorites. *Nat. Geosci.* 41–45, doi: 10.1038/NGEO704.

Lange R. A., Cashman K. V. and Navrotsky A. (1994) Direct measurements of latent heat during crystallization and melting of a ugandite and an olivine basalt. *Contrib. Mineral. Petrol.* **118**, 169–181.

Lange R. A. and Navrotsky A. (1992) Heat capacities of Fe_2O_3-bearing silicate liquids. *Contrib. Mineral. Petrol.* **110**, 311–320.

Langenhorst F. and Poirier (2000) Anatomy of black veins in Zagami: clues to the formation of high-pressure phases. *Earth Planet. Sci. Lett.* **184**, 37–55.

Lapen T. J., Righter M., Andreasen R., Irving A. J., Satkoski A., Beard B. L., Nishiizumi K., Jull A. J. T. and Caffee M. W. (2017) Two billion years of magmatism recorded from a single Mars meteorite ejection site. *Sci. Adv. 3*, 6.

Locock A. 2008. An Excel spreadsheet to recast analyses of garnet into end-member components, and a synopsis of the crystal chemistry of natural silicate garnets. Computers in Geosciences 34:1769–1780.

Ma C., Liu Y. and Tschauner O. (2013) Tissintite, IMA 2013-027. CNMNC Newsletter No. 16, August 2013, page 2707; *Min. Mag.* **77**, 2695–2709.

Ma C., Tschauner O., Lui Y., Beckett J. R., Rossman G. R., Zuravlev K., Prakapenka V., Dera P., Sinogeikin S., Smith J. and Taylor L. A. (2014) Discovery of ahrensite γ-Fe_2SiO_4 and tissintite (Ca, Na,□)$AlSi_2O_6$: two new high pressure minerals from the Tissint martian meteorite. *Lunar Planet Sci XLV*. Lunar Planet Inst., Houston. #1222 (abstr.).

Ma C., Tschauner O. T., Beckett J. R., Liu Y., Rossman G. R., Zhuravlev K., Prakapenka V., Dera P and Taylor L. A. (2015) Tissintite, (Ca, Na, ☐)$AlSi_2O_6$, a highly defective, shock-induced high-pressure clinopyroxene in the Tissint martian meteorite. *Earth Planet. Sci. Lett.* **422**, 194–205.

Ma C., Tschauner O., Beckett J. R., Liu Y., Rossman G. R., Sinogeikin S. V., Smith J. S. and Taylor L. A. (2016a) Ahrensite, *γ*-Fe2SiO4, a new shock-metamorphic mineral from the Tissint meteorite: Implications for the Tissint shock event on Mars. *Geochim. Cosmochim. Acta* **18**4, 240–256.

Ma C. and Tschauner O. (2016b) Discovery of tetragonal almandine, $(Fe,Mg,Ca,Na)_3(Al,Si,Mg)_2Si_3O_{12}$, a new high-pressure mineral in Shergotty. *Meteor. Planet. Sci.* 51 (S1) #6124 (abstr.).

McMillan P.F, Wolf G.H. and Lambert P. (1992) A Raman spectroscopic study of shocked single crystalline quartz. *Phys. Chem. Miner.* **19**, 71–79.

McQueen R. G. 1989. Shock waves in condensed media: Their Properties and the Equations of State of Materials Derived from Them. In *High-pressure equations of state: Theory and Applications*. Edited by Eliezer S. and Ricci R. A. North-Holland: Elsevier Science Publishers. pp. 101-216.

Melosh H. J. 1985. Ejection of rock fragments from planetary bodies. *Geol.* 13, 144–148.

Melosh H. J. 1995. Cratering dynamics and the delivery of meteorites to the earth. *Meteoritics* 30, 545–546.

Mernagh T.P. (1991) Use of the laser Raman microprobe for discrimination amongst feldspar minerals. *J. Raman Spectro.* **22**, 453–457.

Miao S. Q., Li H. P. and Chen G. (2014) Temperature dependence of thermal diffusivity, specific heat capacity, and thermal conductity for several types of rocks. *J. Therm. Anal. Calorim.* **115**, 1057–1063.

Nakazawa S., Watanabe S., Kato M., Iijima Y., Kobayashi T. and Sekine T. (1997) Hugoniot equation of state of basalt. *Planet. Space Sci.* **45**, 1489–1492.

Ohtani E., Kimura Y., Kimura M., Takata T., Kondo T. and Kubo T. (2004) Formation of high-pressure minerals in shocked L6 chondrite Yamato 791384: constrains on shock conditions and parent body size. *Earth Planet Sci. Lett*. **227**, 505–515.

Osako M., Ito E. and Yoneda A. (2004) Simultaneous measurements of thermal conductivity and thermal diffusivity for garnet and olivine under high pressure. *Phys. Earth Planet. Inter.* **143**–**144**, 311–320.

Rauch M., Keppler H., Hafner W., Poe B. and Wokam A. (1996) A pressure-induced phase transition in $MgSiO_3$-rich garnet revealed by Raman spectroscopy. *Am Miner.* **81**, 1289–1292.

Ringwood A.E. and Major A. (1971) Synthesis of majorite and other high-pressure garnets and perovskites. *Earth Planet. Sci. Lett.* **7**, 371–375.

Schertle H.-P., Schreyer W., and Chopin C. (1991) The pyrope-coesite rocks and their country rock at Parigi, Dora Maira Massif, Western Alps: Detailed petrography, mineral chemistry and P-T path. *Contrib. Miner. Petrol.* **108**, 1–21.

Sekine T., Kobayashi T., Nishio M. and Takahashi E. (2008) Shock equation of state of basalt. *Earth Planets Space* **60**, 999–1003.

Sharp T.G. and DeCarli P. S. (2006) Shock effects in meteorites In *Meteorites and the Early Solar System* (eds. D. S. Lauretta and H. Y. McSween Jr.). The University Press, Tucson. pp. 653–678.

Sharp T. G., Xie Z., De Carli P. S. and Hu J. (2015) A large shock vein in L chondrite Roosevelt County 106: Evidence for a long-duration shock pulse on the L chondrite parent body. *Meteor. Planet. Sci.* **50**, 1941–1953.

Shaw C. S. J. and Walton E. L. (2013) Thermal modeling of shock melts in martian meteorites: Implications for preserving martian atmospheric signatures and crystallization of high-pressure minerals from shock melts. *Meteor. Planet. Sci.* **48**, 758–770.

Stähle V., Altherr R., Nasdala L. and Ludwig T. (2011) Ca-rich majorite derived from high-temperature melt and thermally stressed hornblende in shock veins of crustal rocks from the Ries impact crater (Germany). *Contrib. Miner. Petrol.* **161**, 275–291.

Smith J. V. and Mason B. (1970) Pyroxene-garnet transformation in Coorara meteorite. *Science* **168**, 832–833.

Stöffler D., Ostertag R., Jammes C. and Pfannschmidt G. (1986) Shock metamorphism and petrography of the Shergotty achondrite. *Geochim. Cosmochim. Acta* **50**, 889–903.

TrØnnes R. G. and Frost D. J. (2002) Peridotite melting and mineral–melt partitioning of major and minor elements at 22–24.5 GPa. *Earth & Planet. Sci. Lett*. **197**, 117–131.

Tschauner O. Asimow P. D., Kostandova N., Ahrens T. J., Ma C., Sinogeikin S., Liu Z., Fakra S. and Tamura N. (2009) Ultrafast growth of wadsleyite in shock-produced melts and its implications for early solar system impact processes. *Proc. Nat. Acad. Sci.* **106**, 13691–13695. https://doi.org/10/1073/pnas.0905751106.

van de Moortèle B., Reyard B., McMillan P. F., Wilson M., Beck B., Gillet P. and Jahn S. (2007) Shock-induced transformation of olivine to a new metastable $(Mg,Fe)_2SiO_4$ polymorph in martian meteorites. *Earth Planet. Sci. Lett.* **261**, 469–475.

Warren P. H. (1994) Lunar and martian meteorite delivery services. *Icarus* **111**, 338 – 363. Doi: 10.1006/icar.1994.1149.

Walton E. (2013) Shock metamorphism of Elephant Moraine 79001: Implications for olivine-ringwoodite transformation and the complex thermal history of heavily shocked martian meteorites. *Geochim. Cosmochim. Acta* **107**, 299–315.

Walton E.L., Sharp T.G., Hu J. and Filiberto J. (2014) Heterogeneous mineral assemblages in martian meteorite Tissint as a result of a recent small impact event on Mars. *Geochim. Cosmochim. Acta*, **140**, 334–348.

Walton E. L., Tschauner O., Herd C. D. K. and Agee C. B. (2016a) Shock effects in new martian olivine basalt Northwest Africa 10416: Distinct from shergottites but akin to Northwest Africa 8159. 47th Lunar and Planetary Science Conference, Abstract #1639.

Walton E. L., Sharp T. G. and Hu J. (2016b) Frictional melting processes and the generation of shock veins in terrestrial impact structures: Evidence from the Steen River impact structure, Alberta, Canada. *Geochim. Cosmochim. Acta* **180**, 256–270.

Wang A., Jolliff B. L., Haskin L. A., Kuebler K. E. and Viskupic M. (2001) Characterization and comparison of structural and compositional features of planetary quadrilateral pyroxenes by Raman spectroscopy. *Am. Miner.* **86**, 790–806.

Wang C., Yoneda A., Osako M., Ito E., Yoshino T. and Jin Z. (2014) Measurement of thermal conductivity of omphacite, jadeite, and diopside up to 14 GPa and 1000 K: Implication for the role of eclogite in subduction slab. *J. Geophys. Res. Solid Earth* **119**, 6277–6287.

Wieler R., Huber L., Busemann H., Seiler S., Leya I., Maden C., Masarik J., Meier M. M. M., Nagao K., Trappitsch R. and Irving A. J. (2016) Noble gases in 18 martian meteorites and angrite Northwest Africa 7812: Exposure ages, trapped gases and a re-evaluation of the evidence for solar cosmic-ray produced neon in shergottites and other achondrites. *Meteor. Planet. Sci.* **50**, 326–353.

Xie Z. and Sharp T. G. (2007) Host rock solid-state transformation in a shock-induced melt vein of Tenham L6 chondrite. *Earth and Planetary Sci. Lett.* **254**, 433-445

Yang H., Konzett J., Frost D. J. and Downs R. T. (2009) X-ray diffraction and Raman spectroscopic study of clinopyroxenes with six-coordinated Si in the $Na(Mg_{0.5}Si_{0.5})Si_2O_6$-$NaAlSi_2O_6$ system. *Amer. Miner.* **94**, 942–949.

Figures and table captions

Figure 1. Plane light overview of a thin section investigated in this study, showing irregular shock veins (arrows) embedded in a groundmass of transparent crystalline plagioclase, brown pyroxene and opaque olivine + magnetite assemblages.

Figure 2. SEM back-scattered electron (BSE) images of the shock vein investigated in this study. (A) Mosaic of three BSE images, providing an overview of a shock vein with maximum width of ~600 μm. White rectangles indicate the location of BSE images B-D. (B) Higher

magnification image of ahrensite formed from olivine at the shock vein margin. A thick calcite-filled fracture cuts across the shock vein and host rock, and is clearly terrestrial in origin. Maskelynite in the vicinity of the shock vein forms smooth, unfractured crystals (Am-Pl). (C) A higher magnification image of the host-rock / shock-vein contact tissintite as a tranformation product of plagioclase in direct contact with the now-crystallized shock melt and as clasts entrained within the vein (the latter shown in D). (E) Olivine near to the shock veins with a bright, mottled rim, shown as a higher magnification BSE image in Fig. 4. The rim is composed of two phases, identified by Raman and TEM to be clinoenstatite + magnetite. (E) A lithic clast entrained in the shock vein contains tissintite and coesite (Coes). Pyroxene (Px) is untranformed. (G) BSE image of the shock vein interior composed of poikilitic garnet crystals and blocky pyroxene. Several bright blebs of Fe-sulphides are also visible in this image.

Figure 3. Raman spectra taken from areas within the shock vein (left) and olivine transformation products along shock vein margins (right).

Figure 4. Focused Ion Beam (FIB) lift out locations superimposed on BSE images within and surrounding the shock vein. See text for details.

Figure 5. Bright-field TEM images of FIB 1. (a) 200–300 nm size ahrensite crystals formed from olivine in contact with the quench-crystallized shock melt. Stacking faults on {110} are visible in several grains. (b) Garnets intergrown with tetragonal (square) prismatic crystals from near the shock vein margin. Inset CBED pattern of the stishovite [001] zone axis. The irregular shapes of the diffraction discs represent the shape of the residual diffracting core of the damaged crystal. Bright-field TEM image (c) of a rectangular crystal of stishovite. The margin of this grain is amorphous from electron irradiation damage while the center is crystalline and shows numerous defects. (d) Garnet with numerous prismatic stishovite crystals. The inset SAED pattern is indexed as the garnet [111] zone. Gnt = garnet; St = stishovite.

Figure 6. Images of FIB 2. (a) SEM BSE image of large poikilitic garnet (Gnt) with numerous darker inclusions and several bright inclusions of Fe-sulphide. (b) TEM bright field image of the interior of the garnet shown in (a). Inclusions are subrounded to amoeboid-shaped glass (gls).

Figure 7. Bright field TEM images of FIB 3. (a) The mineral assemblage at the center of the 0.6 mm wide shock vein comprises garnet (Gnt) + pyroxene (Px) + Fe-sulfide embedded in glass. Garnet contains a rod-shaped inclusion of stishovite (St). The stishovite crystal is dark because it is diffracting more strongly than the surrounding garnet. The white box shows the location of bright field image (b). (b) Close up of stishovite elongated on [001] and viewed along [110], showing dipyramidal terminations. Inset convergent-beam electron diffraction (CBED) pattern of the stishovite [110] zone axis. (c) Pyroxene grain from which acquired EDX compositional data indicate it is a solid solution between jadeite-hedenbergite. (d) SAED pattern of the pyroxene grain shown in (c) indexes as the clinopyroxene [350] zone axis.

Figure 8. Images of FIB 4 and comparison with olivine decomposition products in Tissint. (a) Overview of FIB 4 with olivine on the right and a symplectic intergrowth of two minerals (pyroxene + magnetite) on the left. These symplectites correspond to the bright and dark grains in BSE images, shown in Figure 4 (FIB 4 location). **(**b) Bright field TEM image of a fine-grained intergrowth of pyroxene and magnetite. The inset convergent-beam electron diffraction (CBED) pattern is of magnetite down [1-14]. (c) Bright field TEM image of pyroxene in the symplectite. The circle denotes the area from which the SAED pattern in (d) was taken, as well as an EDX spot analysis. A d-spacing of 6.47 Å corresponds to 110 of clinoenstatite. (d) For comparison, a clast of olivine entrained within a shock melt pocket in the Tissint shergottite, which has decomposed to bridgmanite + magnesiowüstite is shown. This shock-induced reaction texture is distinct from the olivine → pyroxene + oxide assemblage (a–d) in NWA 8159.

Figure 9. One-dimensional heat-flow models for a 0.6 mm wide shock vein in NWA 8159 with starting temperatures of 2500 K. Each temperature (*T*) – time (*t*) curve represents one locality in the melt vein or adjacent host rock. The numbers next to the curves annotate the distance between the investigated locality and the melt-host rock boundary. Solidus and liquidus temperatures of basalt are taken from Hirose et al. (1999).

Figure 10. (a) Phase diagram for the Mg_2SiO_4 – Fe_2SiO_4 system (Fei and Bertka 1991). The transformation of fayalite (Fa_{75}) to ahrensite requires pressures >8 GPa and <16 GPa at 1600 ^oC, shown by the dashed blue lines. (b) Experimentally-determined phase relations for mid-ocean ridge basalt composition up to 27 GPa from Hirose et al. (1998). The Mj + St assemblage in the shock vein boundary area suggest crystallization above ~16 GPa. In contrast, the Mj + Cpx + St assemblage in the center of the thicker vein (0.6 mm wide) suggests a pressure below 16 GPa. One can reconcile this pressure difference by looking at quench rates (Fig. 9). The shock vein margin (boundary shared with the host rock) quenches very fast and preserves the early history. The vein center quenches more slowly and shows evidence of decreasing pressure during crystallization. The starting pressure was therefore ~16 to 18 GPa and the pressure dropped to below 16 GPa during the 100 ms required to quench the vein center. Mj = majoritic garnet, St = stishovite, Cpx = clinopyroxene, Ca-Pv = Calcium perovskite, Pv = silicate perovskite (bridgmanite).

Table 1. Representative electron microprobe WDS data from olivine, ahrensite and shock vein crystallization products.

Table 2. TEM EDX data for shock vein crystallization products.

Figure 1

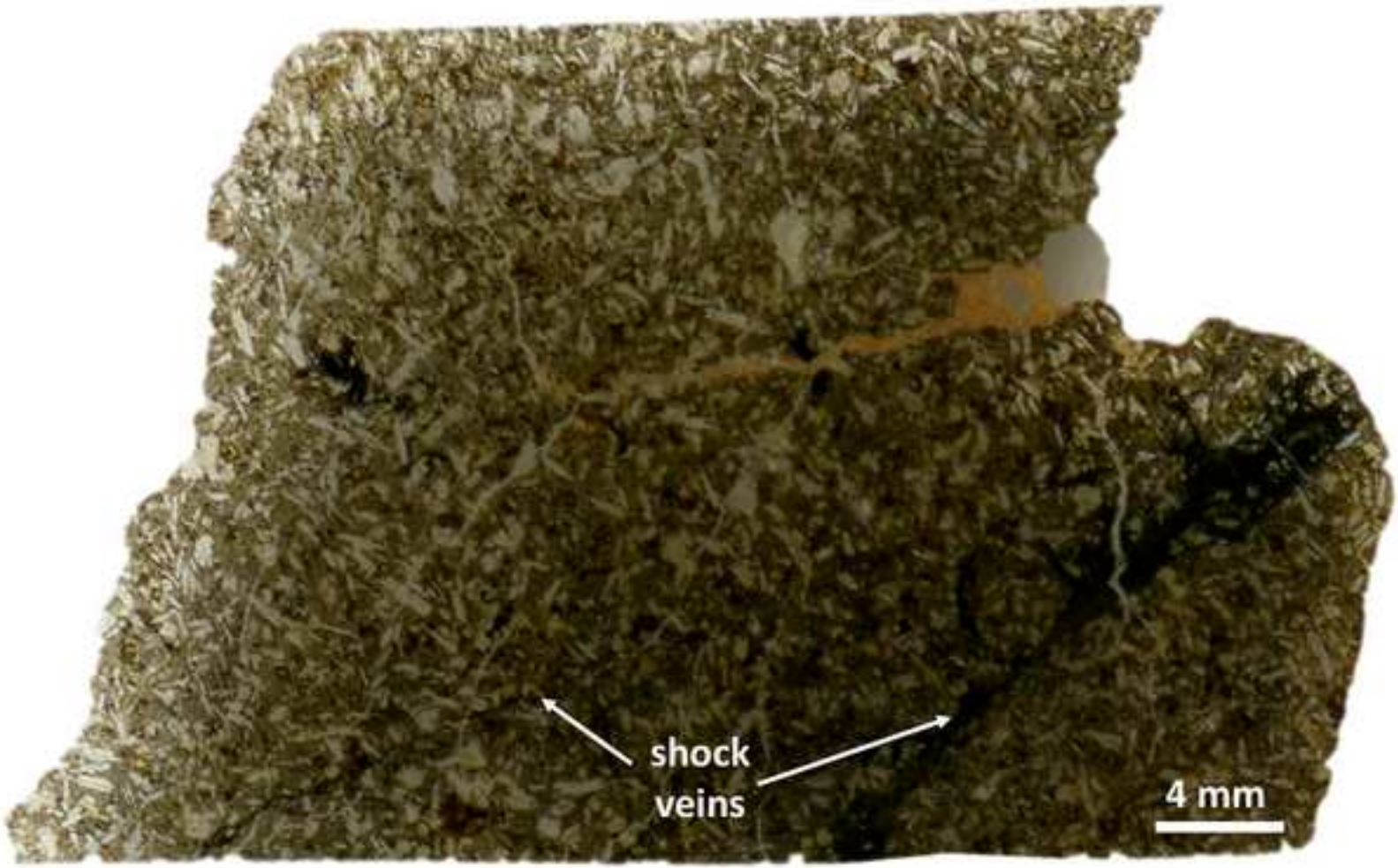

Figure 2: Overview of shock vein and textures

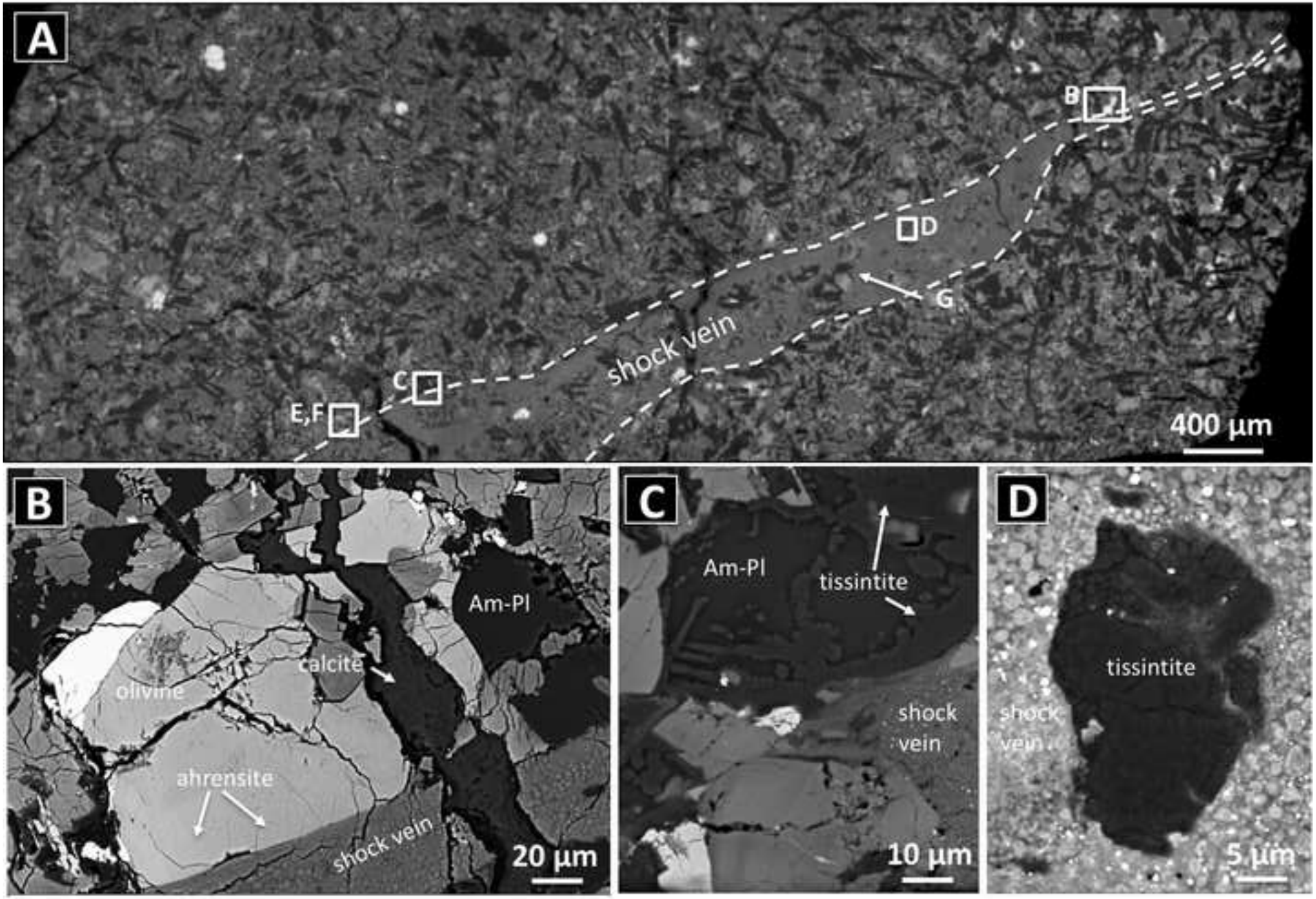

Figure 2 continued

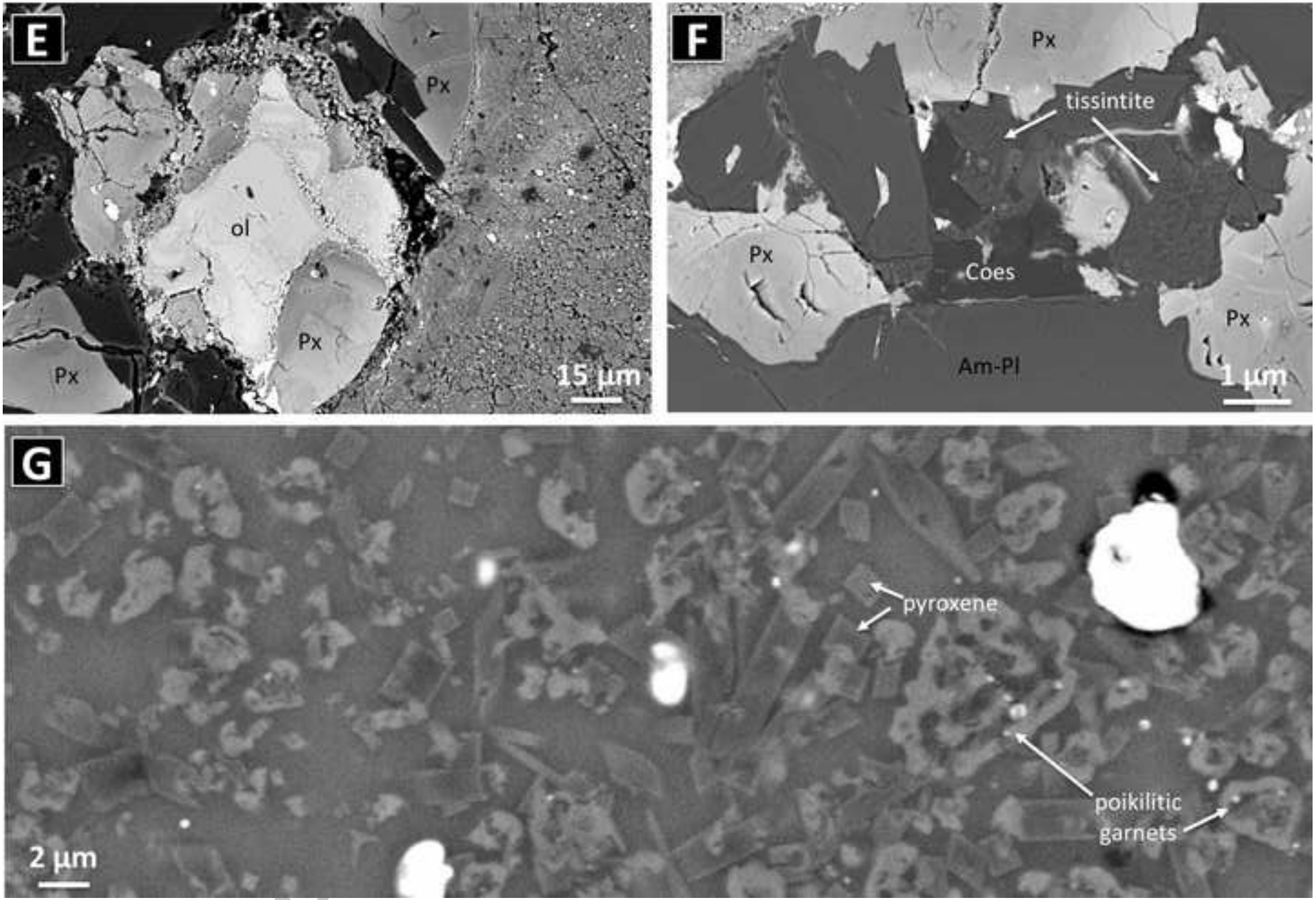

Figure 3

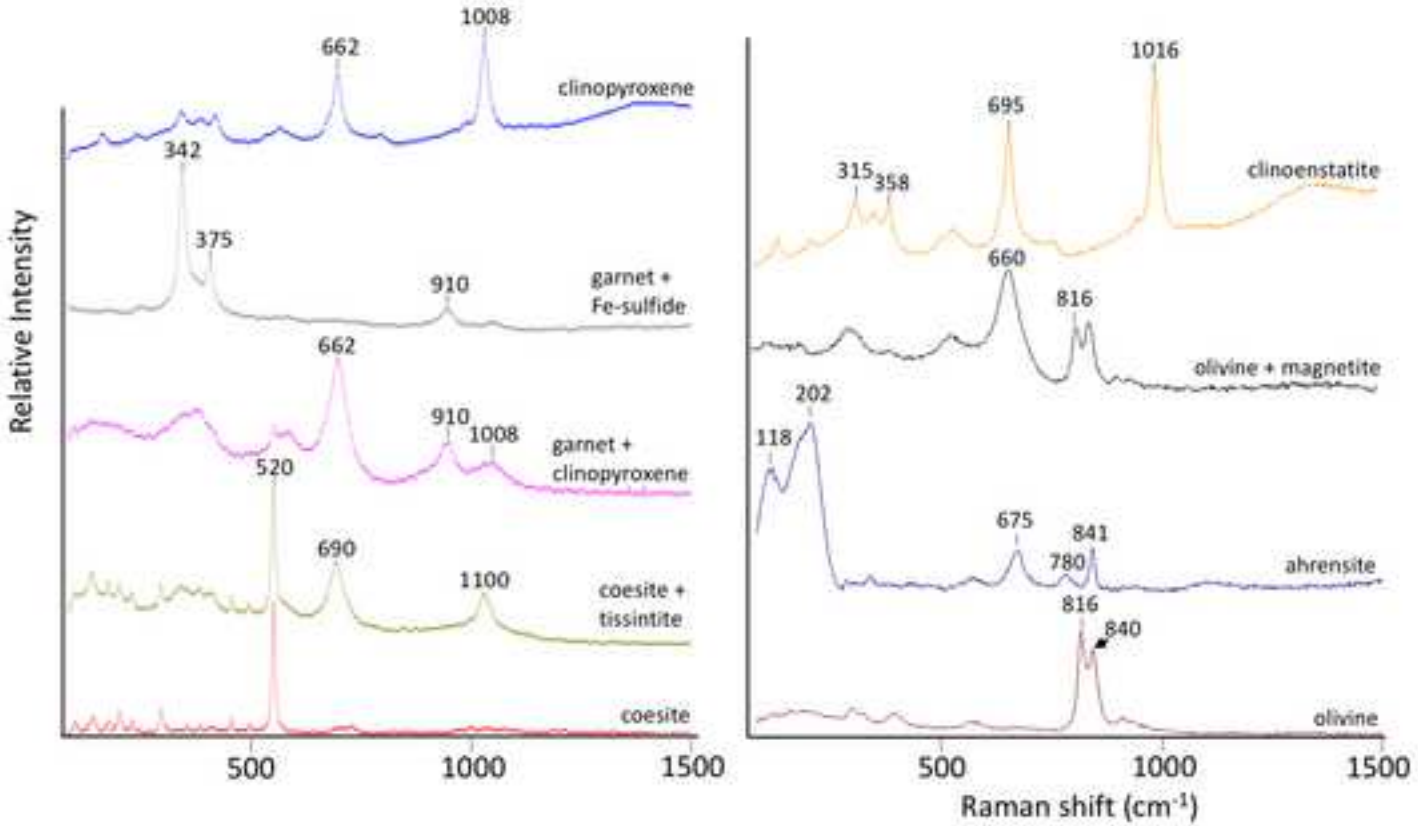

Figure 4 FIB Locations

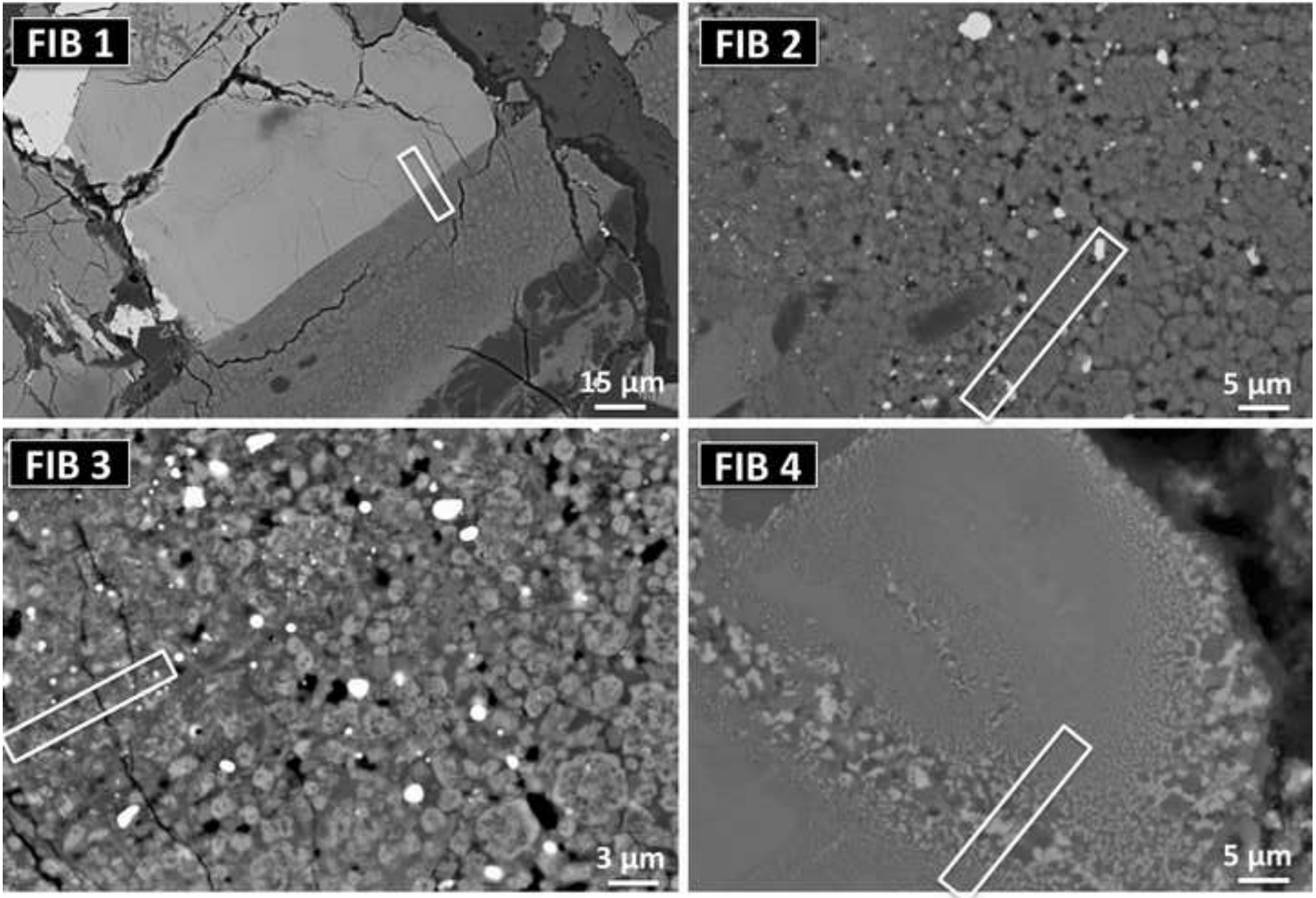

Figure 5

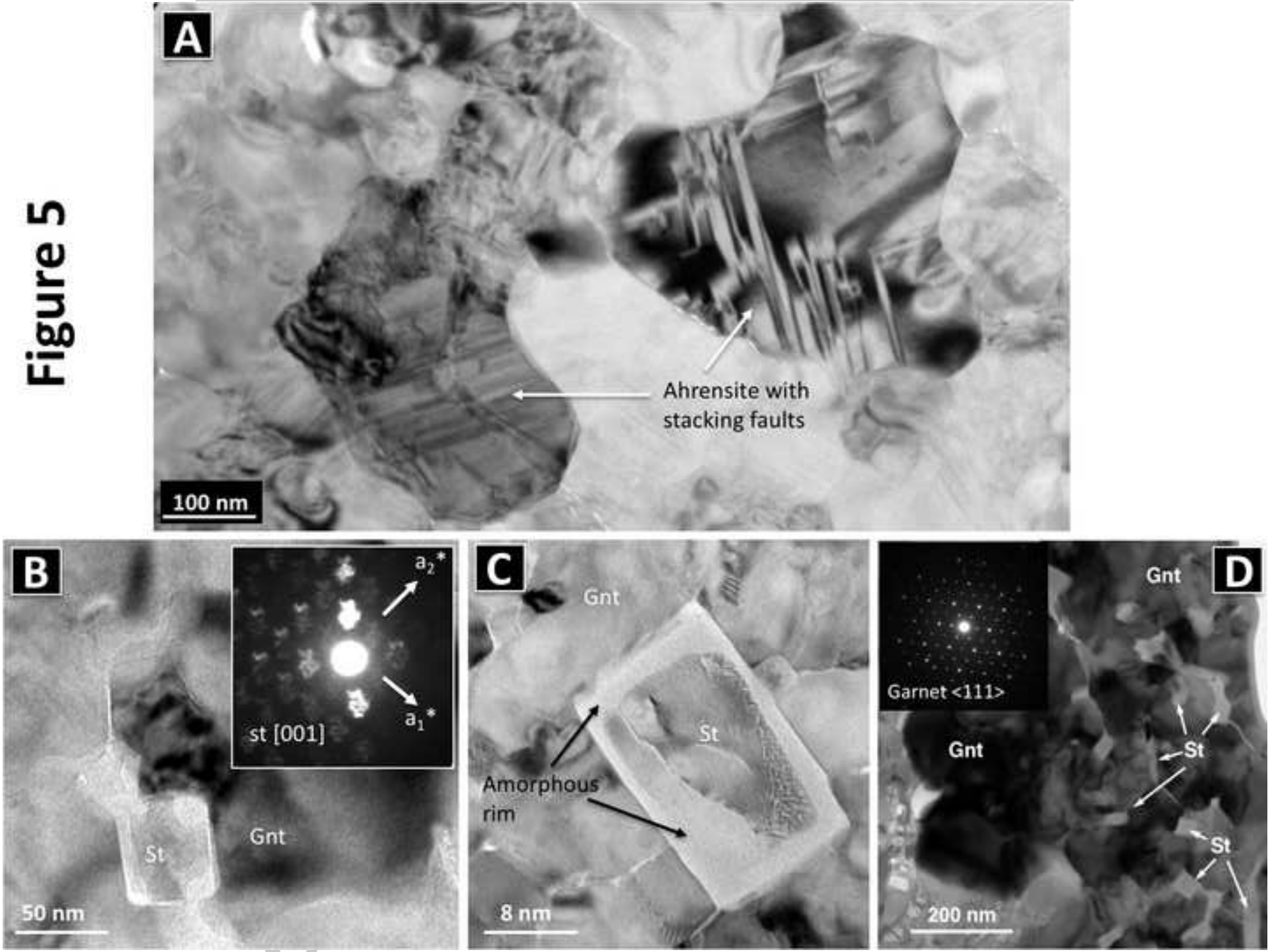

Figure 6

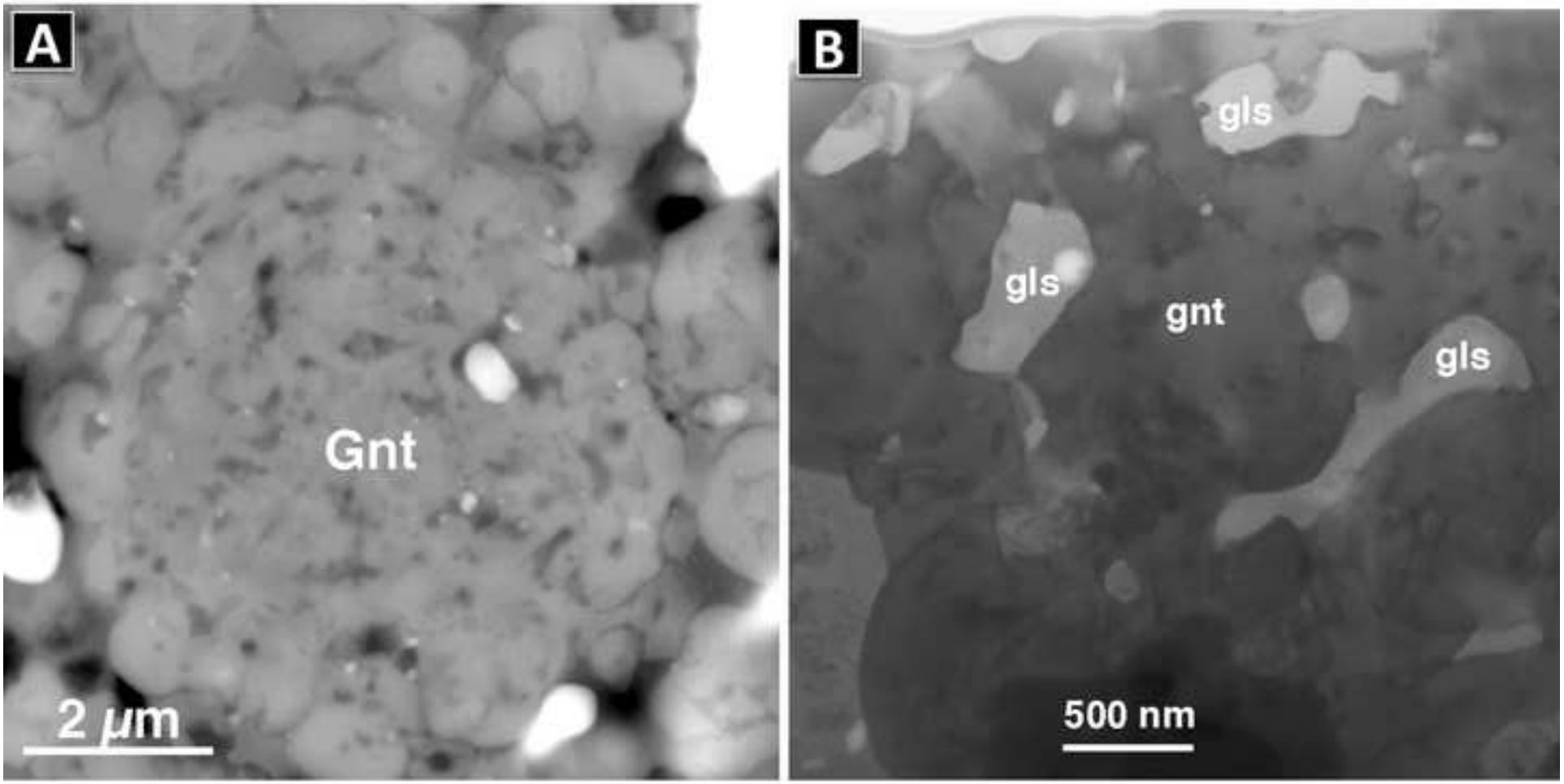

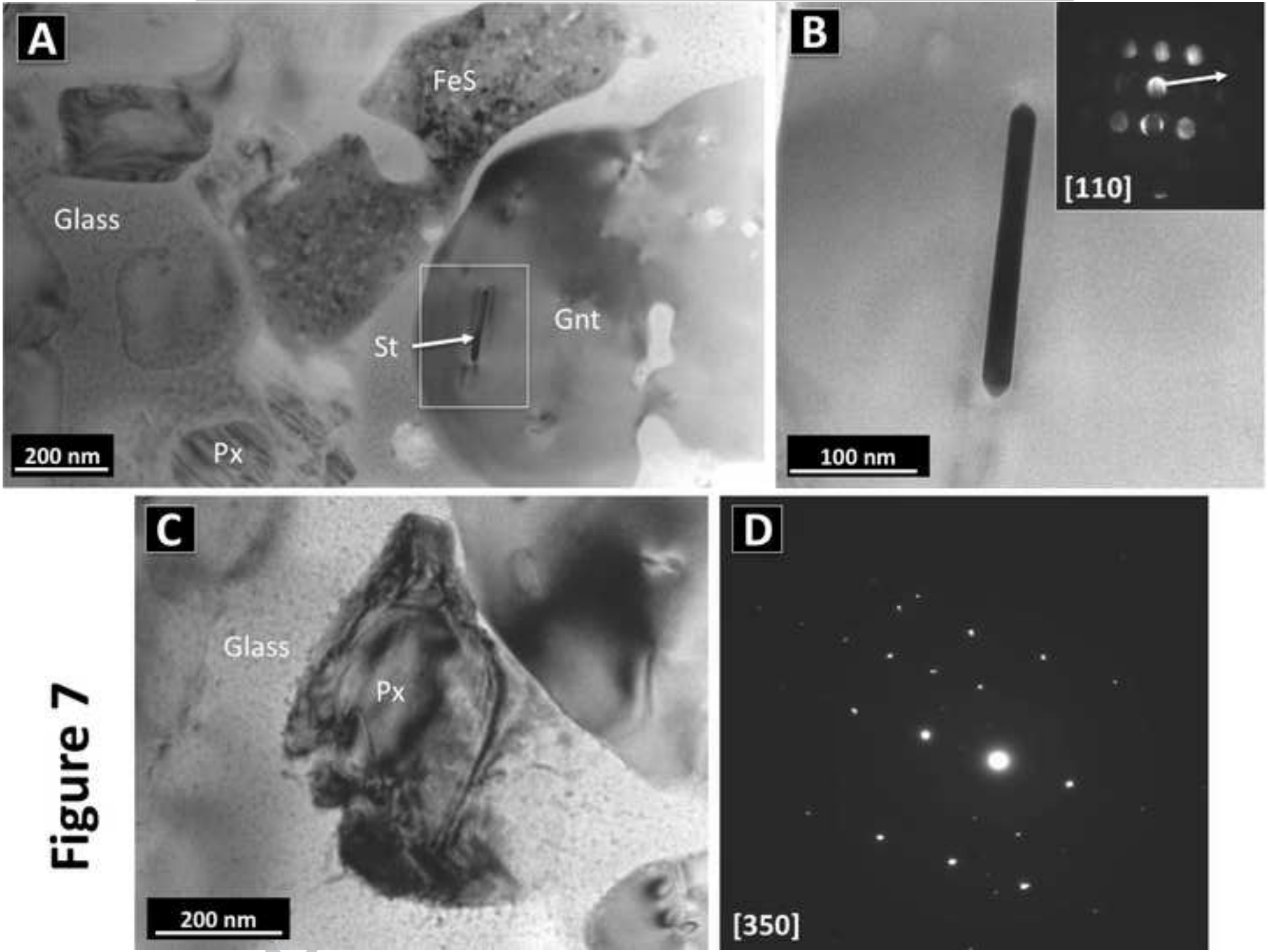

Figure 7

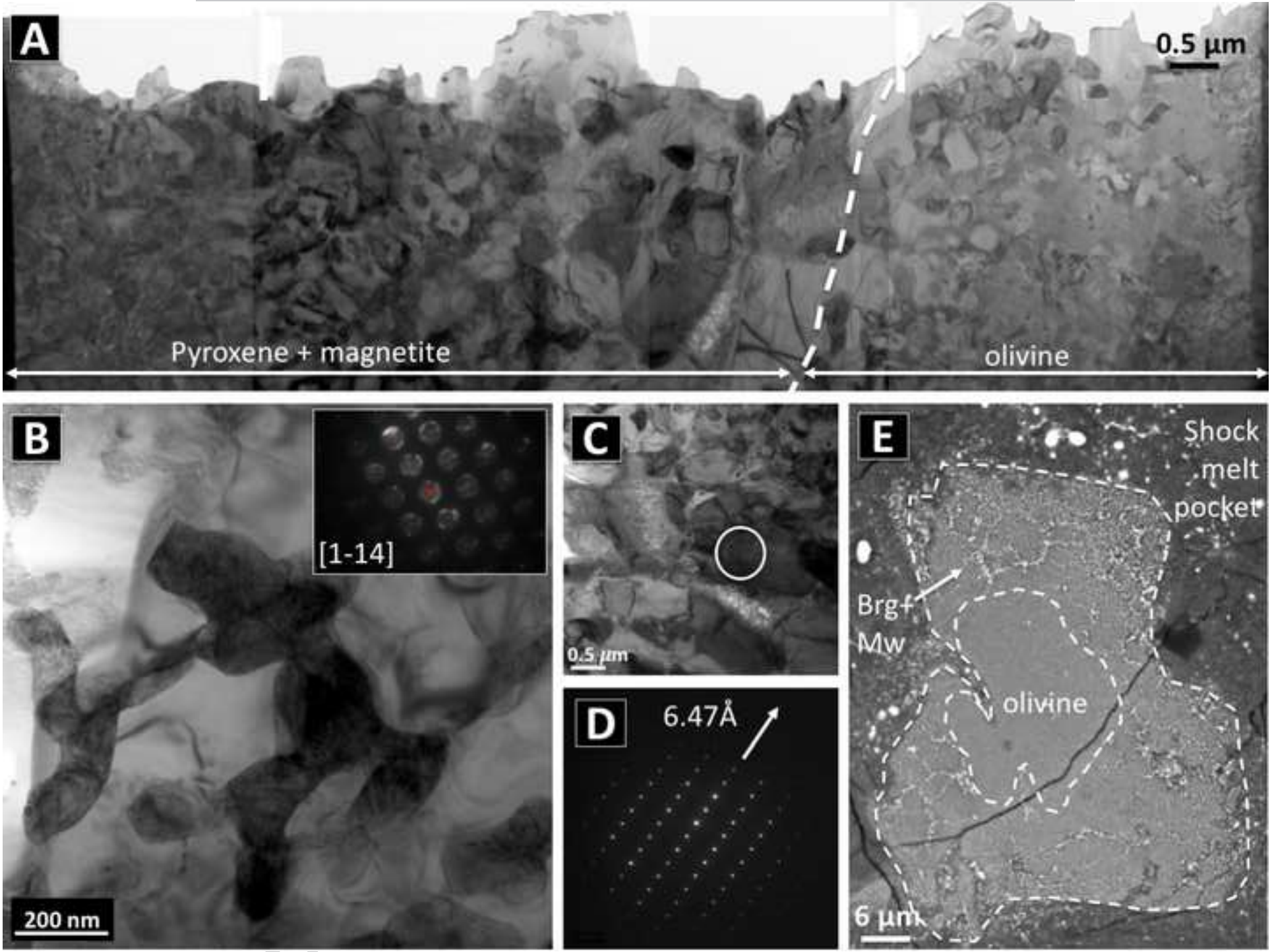

Figure 9

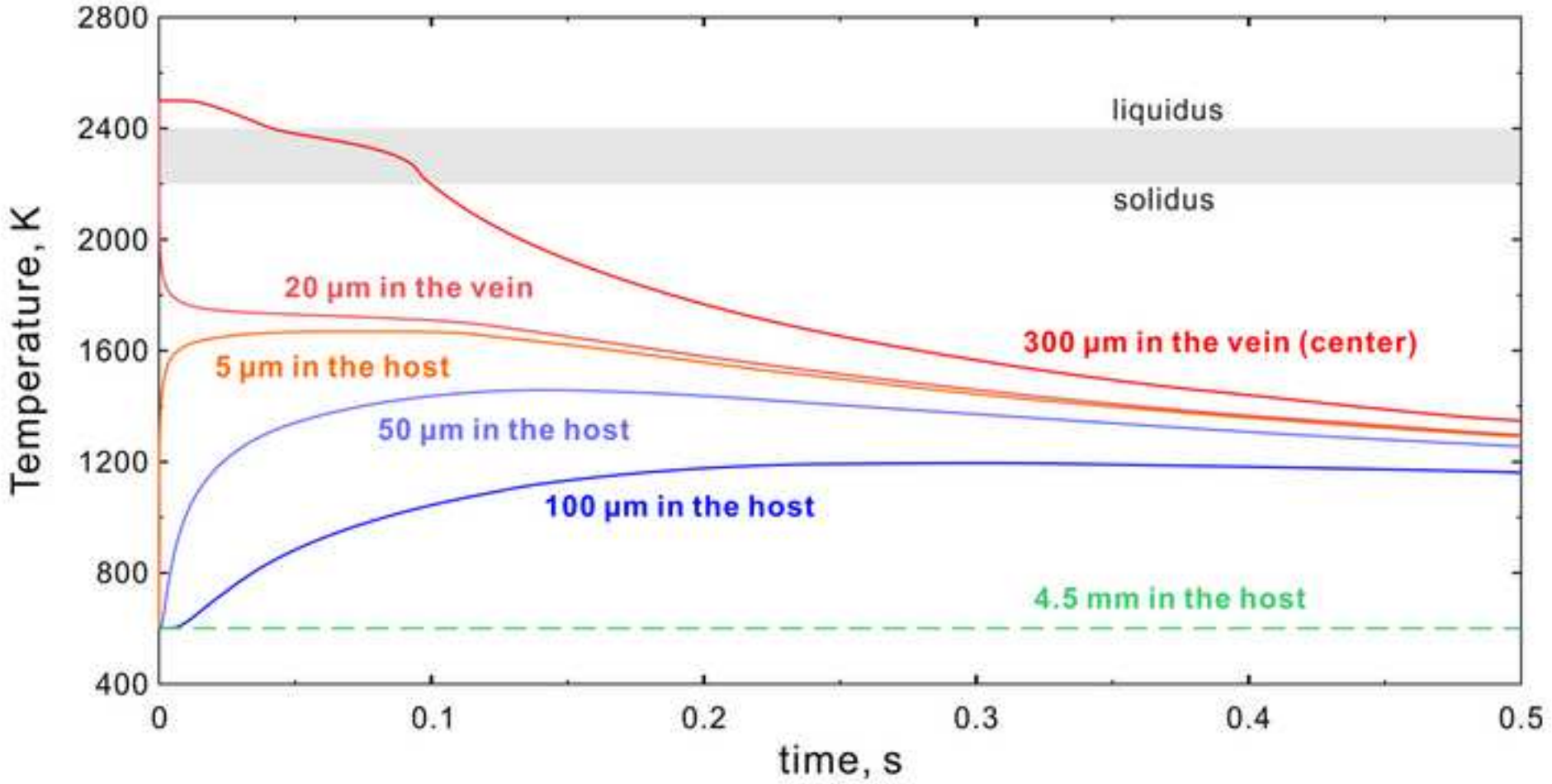

Figure 10

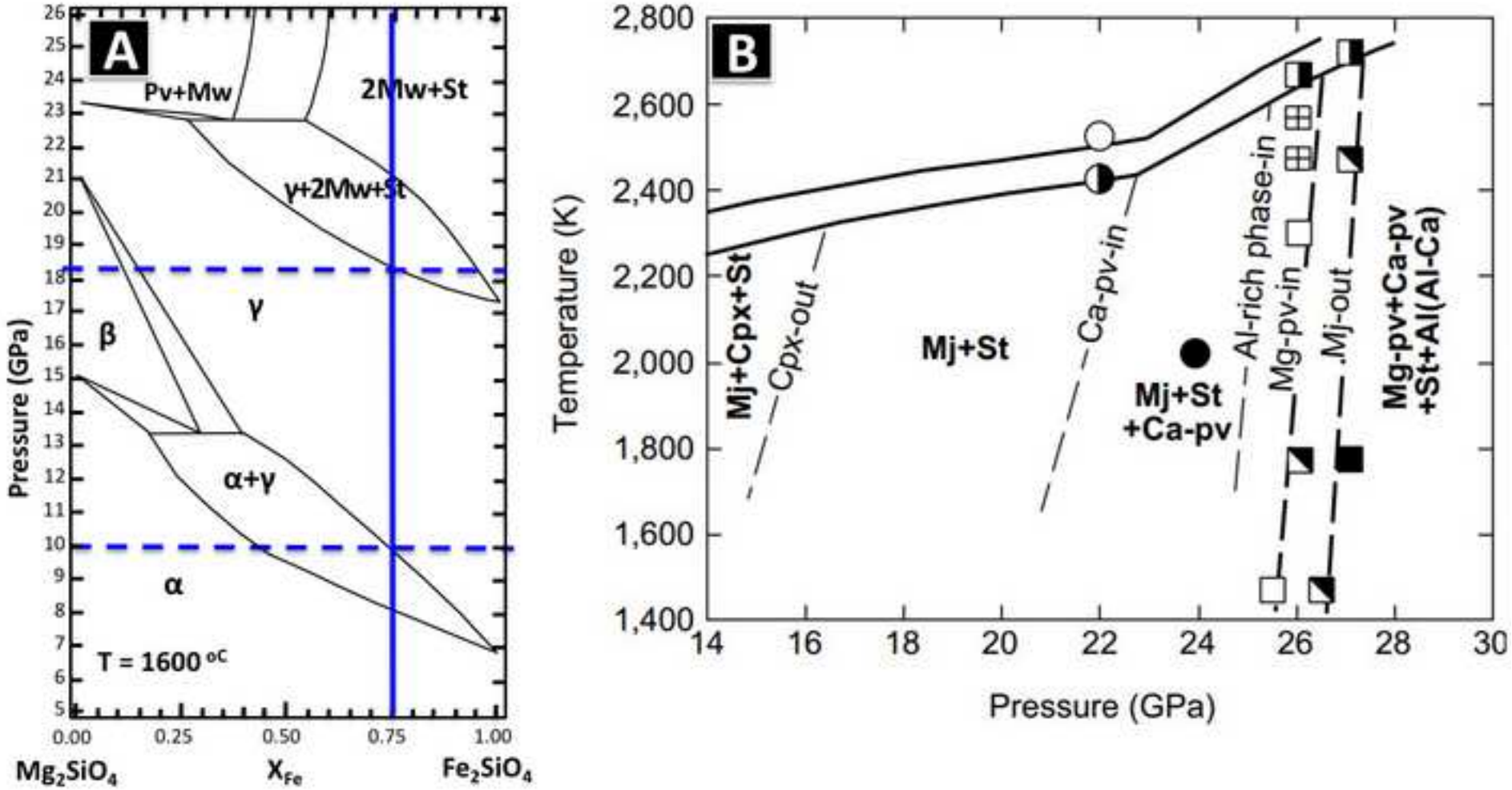

1												
Na_2O	bd	bd	bd	bd	1.59	2.04	1.85	1.88	0.6	4.61	4.36	4.24
K_2O	bd	bd	bd	bd	bd	bd	bd	—	—	0.01	0.02	0.03
Total	100.14	99.60	99.22	99.79	100.45	99.89	99.84	99.94		100.19	100.28	99.74
O =	*4*	*4*	*4*	*4*	*12*	*12*	*12*			*6*	*8*	*8*
Si	0.989	0.989	1.001	0.997	3.484	3.604	3.577			1.8541	2.4245	2.4122
Ti	0.001	0.001	—		0.035	0.034	0.034			0.0005	0.0004	0.0000
Al	0.002	0.003	0.004	0.001	1.223	1.165	1.191			1.1270	1.5603	1.5588
Cr	0.003	0.001	0.002	0.001	0.010	0.007	0.006			0.0010	0.0003	0.0000
Fe^{2+}	1.452	1.431	1.278	1.318	1.628	1.609	1.605			0.0249	0.0225	0.0186
Mn	0.032	0.031	0.021	0.018	0.039	0.029	0.031			0.0005	0.0011	0.0007
Mg	0.496	0.523	0.656	0.645	0.512	0.433	0.410			0.0027	0.0017	0.0000
Ca	0.020	0.021	0.021	0.018	0.829	0.755	0.801			0.4111	0.5904	0.6066
Na	—	—	—	—	0.240	0.308	0.279			0.3138	0.3795	0.3724
K	—	—	—	—	—	—	—			0.0005	0.0012	0.0018
Total	2.995	3.000	2.983	2.988	8.000	7.944	7.935			3.736	4.982	4.971
Fo	74.5	73.1	66.0	67.1								
Garent End Member Recalculation (%)												
majorite					8.6	9.1	9.3					
spessartine					1.3	1.0	1.1					
almandine					41.8	54.3	53.6					
grossular					5.9	3.5	5.2					
skiagite					21.2	20.3	18.9					
NaTi garnet					1.8	1.7	1.7					

na = not analyzed, bd = below detection limits (~0.01-0.02 wt%), end member recalculations using Locock (2008)
Avg = average; the number of garnet spot analyses averaged from electron microprobe (EMP) WDS spot analyses = 18
Garnet-SV = garnet crystallized from melt in the shock vein
Chemical formula for garnet analyses are as follows: garnet-SV 1 = $(Fe_{1.62}Ca_{0.83}Mg_{0.26}Na_{0.23}Mn_{0.04})(Al_{1.22}Si_{0.48}Mg_{0.25}Ti_{0.04}Cr_{0.01})Si_3O_{12}$
garnet-SV 2 = $(Fe_{1.61}Ca_{0.75}Na_{0.31}Mg_{0.24}Mn_{0.03})(Al_{1.16}Si_{0.60}Mg_{0.20}Ti_{0.03}Cr_{0.01})Si_3O_{12}$
garnet-SV 3 = $(Fe_{1.60}Ca_{0.80}Na_{0.28}Mg_{0.22}Mn_{0.03})(Al_{1.19}Si_{0.58}Mg_{0.19}Ti_{0.03}Cr_{0.01})Si_3O_{12}$
*EMP WDS data for tissintite, plagioclase and maskelynite in NWA 8159 from Herd et al. (2017)

2

Table 2. Representative transmission electron microscopy EDX data.

		garnet-SV	stishovite	Px
	1	avg		
O =	*12*	*12*	*2*	*6*
Si	3.36	3.38	0.96	2.03
Ti	nd	0.04	nd	nd
Al	1.30	1.31	0.04	0.33
Fe^{2+}	1.54	1.64	0.01	0.73
Mn	0.04	0.04	nd	nd
Mg	0.61	0.42	nd	0.16
Ca	0.89	0.83	nd	0.32
Na	0.37	0.34	nd	0.43
Total	8.11	8.00	1.01	4.00

nd = not detected

TEM EDX data has been normalized to 100.

Avg = average; the number of garnet spot analyses averaged for TEX EDX = 8

Garnet-SV = garnet crystallized from melt in the shock vein